JGR Oceans

RESEARCH ARTICLE
10.1029/2019JC015001

Key Points:
- Characterization of the Burdwood Bank circulation
- Burdwood Bank is a site of highly energetic mixing and upwelling
- Tides are the main circulation driver

Supporting Information:
- Supporting Information S1
- Movie S1
- Movie S2

Correspondence to:
R. P. Matano,
rmatano@coas.oregonstate.edu

Citation:
Matano, R. P., Palma, E. D., & Combes, V. (2019). The Burdwood Bank circulation. *Journal of Geophysical Research: Oceans*, *124*. https://doi.org/10.1029/2019JC015001

Received 28 JAN 2019
Accepted 25 AUG 2019
Accepted article online 1 SEP 2019

The Burdwood Bank Circulation

Ricardo P. Matano[1], Elbio D. Palma[2,3], and Vincent Combes[1]

[1]College of Earth, Ocean, and Atmospheric Sciences, Oregon State University, Corvallis, OR, USA, [2]Departamento de Física, Universidad Nacional del Sur, Bahia Blanca, Argentina, [3]Instituto Argentino de Oceanografía/CONICET, Bahia Blanca, Argentina

Abstract A suite of high-resolution numerical simulations characterizes the oceanic circulation in the Burdwood Bank, a shallow seamount located in the northeastern end of the Drake Passage. Model analysis shows energetic upwelling and mixing uplifting deep and benthic waters into the photic layer. Tides and the Antarctic Circumpolar Current are the primary drivers of the bank's circulation. Tidal forcing is the main driver for the entrainment of deep waters into the upper layers of the bank and local wind forcing for the detrainment of these waters into the deep ocean. Passive tracer diagnostics suggest that the dynamical processes triggered by the Burdwood Bank could have a significant impact on local ecosystems and the biogeochemical balance of the southwestern Atlantic region, which is one of the most fertile portions of the Southern Ocean. Model results are robust—they are reproduced in a wide array of model configurations—but there is insufficient observational evidence to corroborate them. Satellite color imagery does not show substantial chlorophyll blooms in this region but it shows strong phytoplankton plumes emanating from the bank. There are several potential explanations for the chlorophyll deficit, including lack of light due to persistent cloud cover, deep mixing layers, fast ocean currents, and the likelihood that blooms, while extant, might not develop on the surface. None of these possibilities can be confirmed at this stage.

Plain Language Summary The Burdwood Bank is a small seamount located in the northeastern portion of the Drake Passage. Model simulations show energetic and persistent uplifting of deep waters in this site. These waters are potentially rich in micronutrients and might contribute to the fertilization of the upper layers of the Southern Ocean. Model analysis indicates that tidal forcing is the main driver for the entrainment of deep waters into the upper layers of the bank and local wind forcing for the detrainment of these waters into the deep ocean.

1. Introduction

The Burdwood Bank (BB; 55°S, 59°W) is a shallow seamount with a rich ecosystem located in the northeastern portion of the Drake Passage (Figure 1). It is separated from the Patagonian shelf by a relatively narrow and shallow channel—90 km wide and 400 m deep—known as the Malvinas Embayment that widens and deepens as it merges with the Malvinas Chasm (Figure 1). The BB is 300 km long and 60 km wide. Its 200-m-deep summit features smaller protuberances, some of which reach to within 50 m of the surface. Its highly productive ecosystem is an important migration destination for a wide variety of seabirds and marine mammals and has been recently declared a marine sanctuary (Namuncura Marine Protected Area; Schetjer et al., 2016). Highly productive bank ecosystems are usually associated with circulation features that promote fertilization (Boehlert & Genin, 1987; Chen et al., 2001; Genin & Boehlert, 1985; White & Mohn, 2004). There are, however, no prior studies of the BB circulation. Piola and Gordon (1989) reported that upon encountering the BB the Antarctic Circumpolar Current (ACC) splits into two branches, which wrap around the bank's edges. A similar feature is observed in satellite data (Figure S1). Piola and Gordon also observed an outcropping of isopycnals at the bank's sides, which they associated with the winter formation of a denser variety of Antarctic Intermediate Waters. Guerrero et al. (1999) highlighted the weak stratification of the waters around the BB, which is sustained by the advection of a lighter type of intermediate waters.

The impact of seamounts on surrounding waters includes retention, mean flow rectification, upwelling, and mixing, all phenomena affecting the local marine ecosystems. Because of the large number of seamounts, more than 30,000 in the North Pacific alone, the effect of seamounts on local dynamics has global consequences (Rogers, 1994). Climate scientists, in particular, are interested in seamount impacts on ocean mixing. Ledwell et al. (2000), for example, reported that vertical diffusivity over the Brazil Basin seamounts

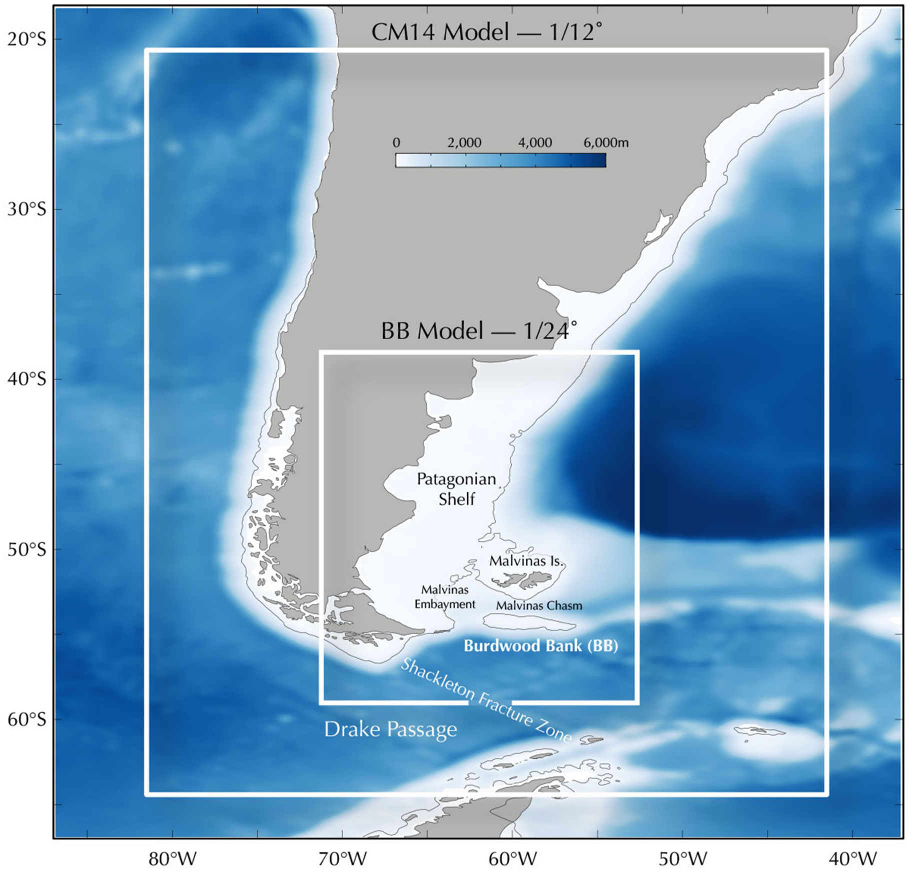

Figure 1. Model domain. Geographical domain of the two models used in this study. CM14 has a horizontal resolution of 1/12° and BB 1/24°. CM14, in turn, is double nested into a 0.25° resolution southern hemisphere model (Combes & Matano, 2014a, 2014b). Color bar represents the bottom depths (in m).

increase by an order of magnitude. Lueck and Mudge (1997) reported even larger increments, 2 to 5 orders of magnitude, over the Cross Seamount in the North Pacific. Toole et al. (1997) found similar results for the Fieberling Guyot in the eastern North Pacific. In addition to their impact on marine ecosystems and the oceanic circulation, seamounts also affect sediment distributions (Roberts et al., 1974; Von Stackelberg et al., 1979).

Earlier seamount studies focused on the formation of Taylor caps, which are regions with relatively stagnant fluid surrounded by vortices (Schär & Davies, 1988), the spin-up of trapped and internal waves and the generation of rectified mean flows (Brink, 1989; Chapman & Haidvogel, 1992; Huthnance, 1978). There are numerous physical and biological studies on the Georges Bank, a highly productive seamount located in the Gulf of Maine (Butman et al., 1982; Chen & Beardsley, 1998; Loder, 1980; Lynch et al., 1996; Naimie et al., 1994). Wright and Loder (1985) reported a significant amplification of flow speeds over the Georges Bank due to the generation of tidal residual currents. Chen et al. (1995) posited that strengthening of cross-bank density gradients during summer should intensify the tidal residual circulation. Franks and Chen (1996) concluded that the steep topography of the northern flank of the bank enhances primary production. Other seamounts have been less studied. Beckmann and Haidvogel (1997) observed amplified diurnal tidal currents and the formation of a trapped anticyclonic vortex over the Fieberling Guyot, a large and elongated seamount located in the North Pacific. Mohn & Beckmann (2002) concluded that density and velocity structures over the Great Meteor Seamount, which is located at the critical diurnal tide latitude, are maintained by rectification of coastally trapped waves. There are few studies on southern hemisphere seamounts. Beckmann et al. (2001) reported that the presence of the Maud Rise, in the Weddell Sea, reduces sea ice formation leading to the formation of polynyas. Meredith et al. (2003) related a chlorophyll patch over the Northwest Georgia Rise (a seamount located in the Scotia Sea) to a localized upwelling cell associated with the formation of a Taylor cap.

In this article we use a suite of model simulations to characterize the circulation over the BB and identify the physical processes underlying its rich and diverse marine ecosystem. Section 2 describes model configuration and experimental setup. Subsequent sections discuss model results.

2. Model Description

The regional model used in this study, henceforth referred as the BB model, has been described in some detail in Matano and Palma (2018), and references therein. For completeness, we include a summary description of its most important characteristics. The BB domain extends from 58° to 38°S and from 69° to 54°W with 1/24° horizontal resolution (Figure 1). Vertically the model equations are discretized into 40 sigma levels, with higher vertical resolution in the top and bottom layers. The bottom topography was derived from the ETOPO1 (1′ resolution; Amante & Eakins, 2009), which was smoothed to minimize the pressure gradient errors associated with terrain-following coordinates.

A combination of radiation and advection conditions is imposed at the open boundaries of the model (Marchesiello et al., 2001). In our most realistic experiment (CTRL) the model is forced with amplitudes and phases of the M_2 tide interpolated from a global TP0X6 tidal model (Egbert et al., 1994) and the climatological values of temperature, salinity, and velocity fields are extracted from a regional model of the entire southwestern Atlantic region at 1/12° horizontal resolution (Combes & Matano, 2014a, 2014b, CM14 hereafter). Further description of the CM14 model, including comparison with in situ and satellite observations, is presented in Combes and Matano (2014a, 2014b, 2018), Matano et al. (2014), Combes and Matano (2019) and Strub et al. (2015). Ancillary analysis of the BB model in other portions of the Patagonian shelf is presented in Matano and Palma (2018).

At the surface the BB model is forced with monthly mean wind stresses extracted from the 1999–2012 Quikscat-ASCAT climatology and heat and freshwater fluxes derived from the Comprehensive Ocean-Atmosphere Data Set (Da Silva et al., 1994). The heat flux also includes a tendency restoring term to the SST climatology derived from the CM14 model following the procedure described in Barnier (1998). Vertical mixing is parameterized with a K-Profile Parameterization scheme (Large et al., 1994) and bottom friction follows a quadratic formulation. There is no explicit horizontal mixing included in the model simulations.

The CTRL experiment was initialized with the CM14 January climatology and subsequently integrated for five years. Model fields from the last year of integration were used for the subsequent analysis of the circulation. Several sensitivity experiments were conducted to identify the contribution of key environmental variables (stratification and bottom topography) and different forcing mechanisms (ACC, local winds, and tides) to the BB circulation (Table 1). Additional experiments were also developed to identify and characterize the transport pathways of ocean and BB waters using a passive tracer advection-diffusion equation and the tracking of passive particles.

Table 1
Characteristics of the numerical experiments described in the text. Sfluxes = Surface fluxes, Bfluxes= Open Boundary fluxes

	Initial Stratification	Forcing	Obs
CTRL	WOA	Tides, Winds, Sfluxes & Bfluxes	Seasonal surface and boundary forcing
3DWND	“	“	3-day average winds
TRNC	“	“	BB truncated at h = 200 m
ACC&TIDES	“	Tides, Sfluxes & Bfluxes	No Winds
ACC&WINDS	“	Winds, Sfluxes & Bfluxes	No Tides
ACC_ONLY	“	Sfluxes & Bfluxes	No tides or winds
STRATz	T(z) & S(z)	Tides and constant Sfluxes	No winds or Bfluxes
TIDES_ONLY	T & S constant	Tides, no Sfluxes or Bfluxes	Barotropic, no winds
WINDS_ONLY	“	Winds, no Sfluxes or Bfluxes	Barotropic, no tides
TIDES&WINDS	“	Tides+winds, no Sfluxes or Bfluxes	Barotropic

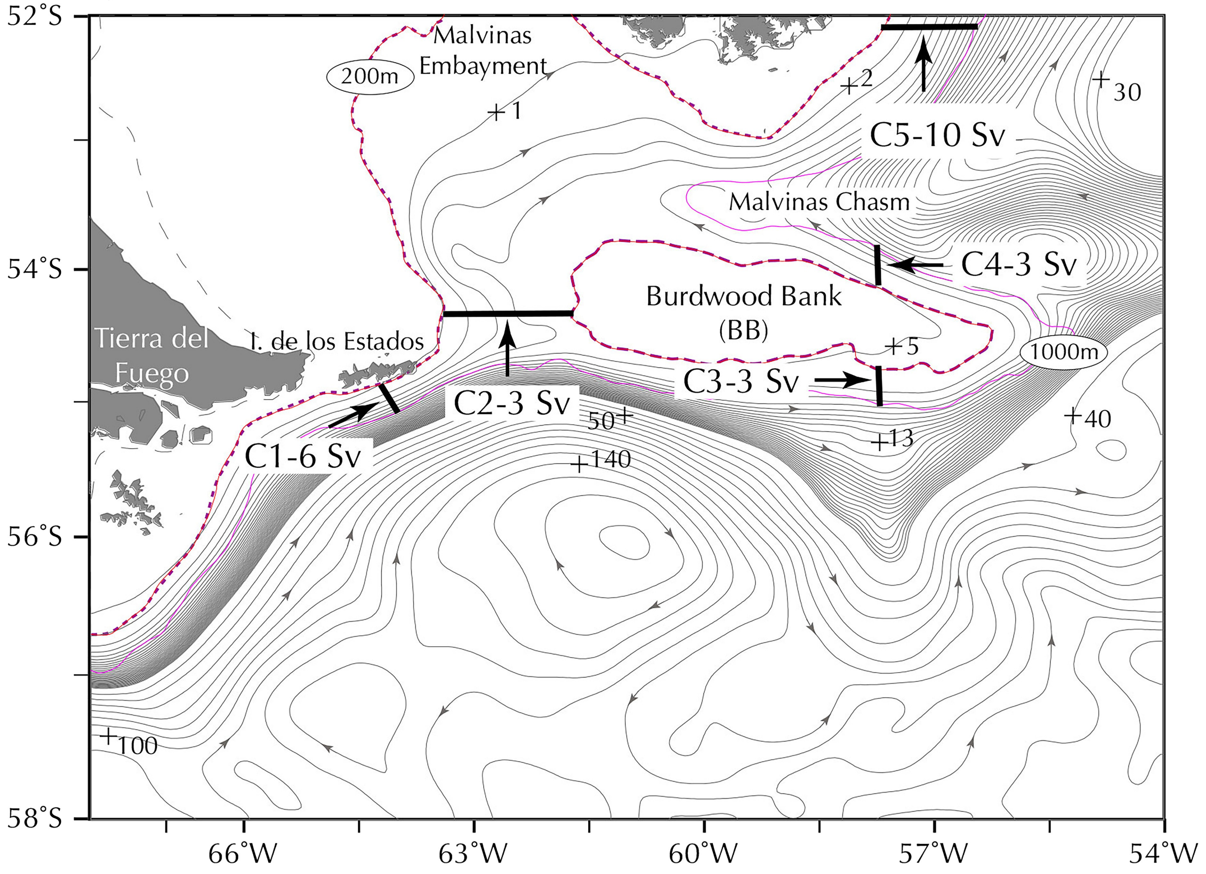
a) Time mean stream function

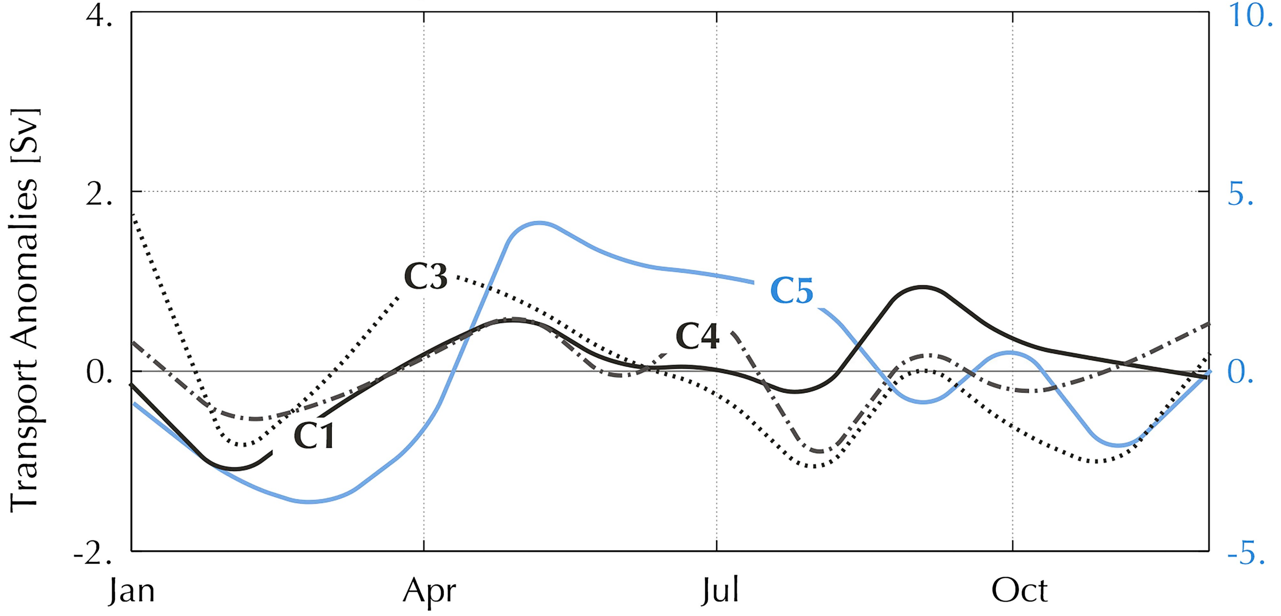
b) Seasonal transport anomalies

Figure 2. CTRL stream function. Top panel shows the time mean stream function of CTRL; contours are in Sverdrups (1 Sv= 10^6 m^3/s) Red contours in top panel mark the 200- and 1,000-m isobaths. Bottom panel shows the seasonal anomalies of the volume transport through the different cross sections marked in the top panel. Anomalies are defined as the climatological monthly value minus the time mean.

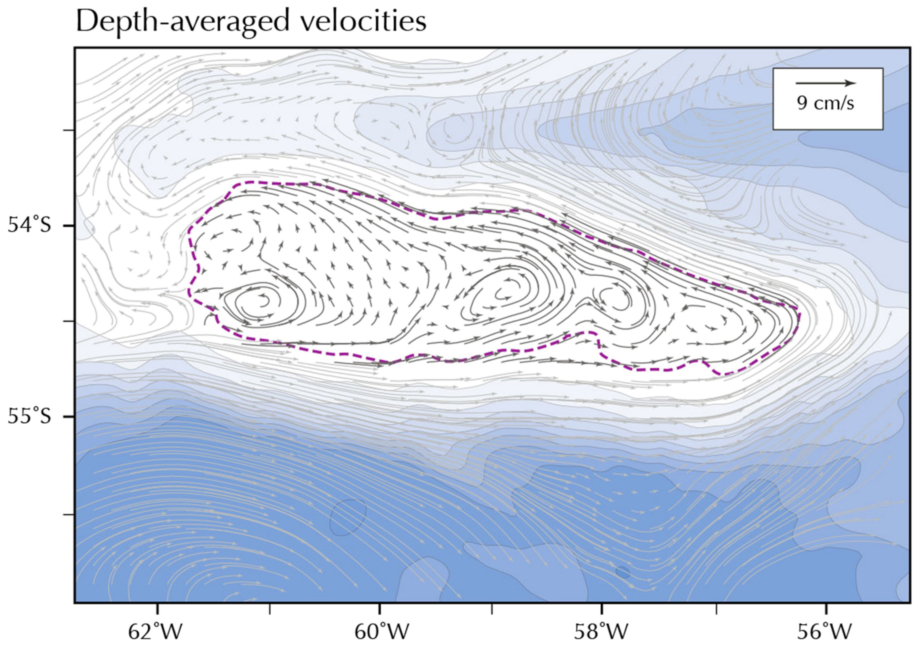

Figure 3. Circulation over the Burdwood Bank (BB). Vectors represent time mean, depth-averaged velocities. Background colors represent bottom topopography. The magenta dotted contour marks the 200-m isobath.

3. Results

3.1. Benchmark Experiment

Experiment CTRL is the benchmark that will be used to establish the characteristics of the circulation over the BB and its connection to the deep ocean region.

3.1.1. Time Mean Circulation

Circulation in CTRL is dominated by the eastward flow of the ACC, which, after crossing the Shackleton Fracture Zone (Figure 2a), diverts most of its volume transport to the north, thus generating an intense eastward jet that advects ~100 Sv past the BB and into the western portion of the Argentinean Basin (Figure 2a). The inshore portion of this jet, here defined by the 200- and 1,000-m isobaths, transports 6 Sv of Antarctic waters to the tip of Isla de los Estados (Section C1; Figure 2a). From there, it bifurcates into a northward branch transporting ~3 Sv into the Malvinas Embayment (Section C2; Figure 2a) and an eastward branch carrying the remainder around the BB (Section C3; Figure 2a). Both branches rejoin in the northern portion of the Malvinas Chasm, feeding the nascent flow of the Malvinas Current (Sections C4 and C5; Figure 2a). The transport in the northernmost section (C5) is augmented by other contributions to reach a value of 10 Sv. The interaction of the ACC with the BB generates a cyclonic recirculation cell, centered at approximately 56°S, 61°W, followed to the east by an anticyclonic meander. Model animations show the intermittent formation of anticyclonic eddies in this region (Movie S1 in the supporting information). Similar features can be observed in animations of AVISO SSH data (Movie S2). Most eddies formed along the southern rim of the BB migrate to the northwest where they are entrained into the equatorward flow of the Malvinas Current. The circulation patterns produced by the model appear to be robust, as they are quite similar to those inferred from hydrographic observations collected nearly 30 years ago (Piola & Gordon, 1989) and current satellite data (Figure S1).

Over the BB there is a broad anticyclonic current along the bank's rim and interior anticyclonic vortexes on top of shallow seamounts (Figure 3). Strong cross-isobath flows are observed near the limit of the summit (200-m isobath), particularly in the southwestern region (Figure 3). Circulation patterns similar to those just reported have been observed in other seamount regions (Beckmann & Mohn, 2002; Haidvogel et al., 1993). The intensification of the circulation toward the seamount's rim is likely to be associated with nonlinear processes, including the rectification of coastally trapped waves and the generation of tidal residual currents (Brink, 1989; Chapman & Haidvogel, 1992; Chen & Beardsley, 1995; Haidvogel et al., 1993).

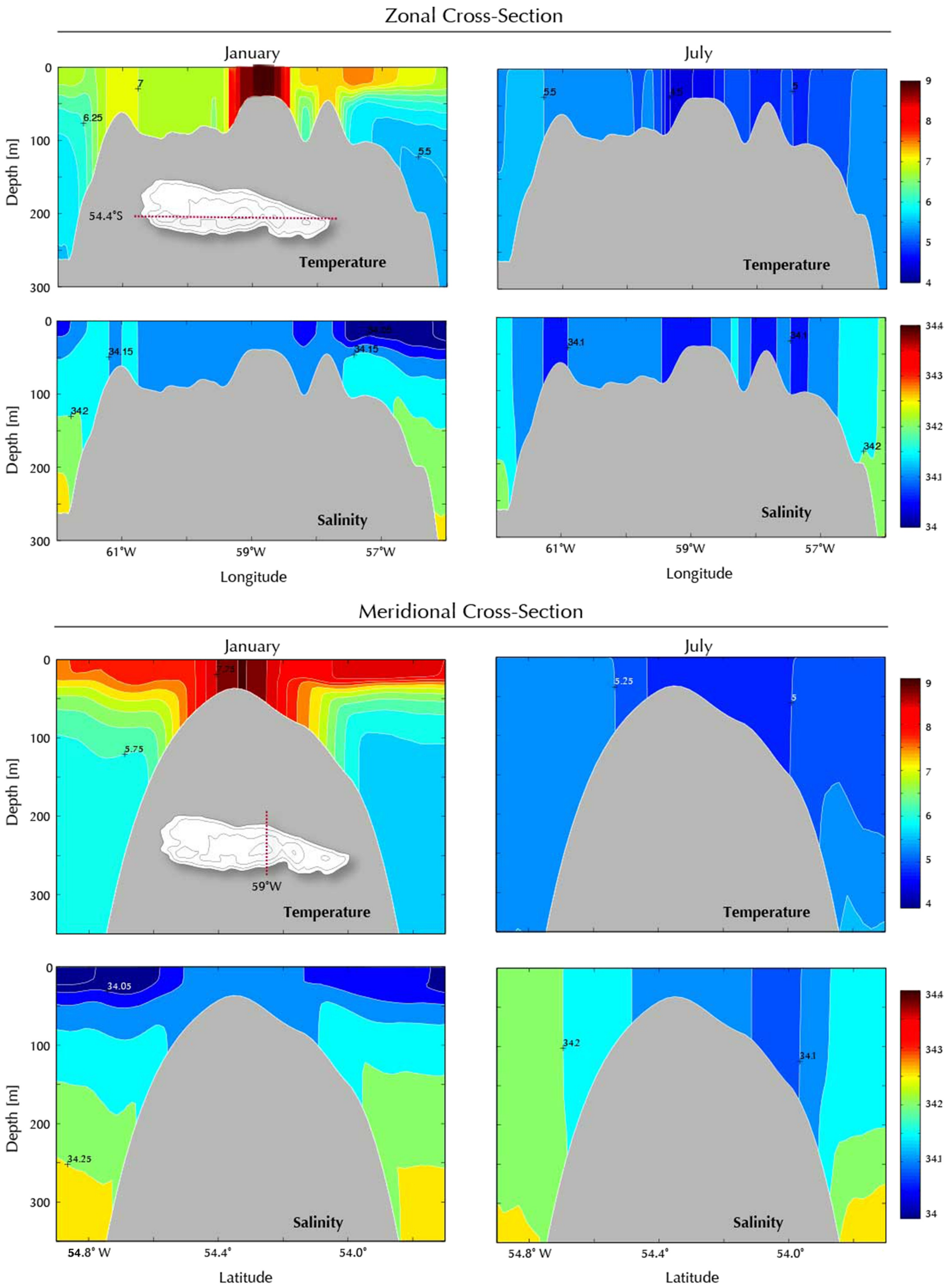

Figure 4. Temperature and Salinity. Zonal (top) and meridional (bottom) cross-sections of temperature and salinity over the BB during the austral summer (January, left) and austral winter (July, right). Location of the cross-sections is shown on the inserts of the top left panel.

While lack of observations hinders evaluation of the model's realism, qualitative agreements between hydrographic and satellite observations do exist (e.g., Piola & Gordon, 1989, Figure 3; Figure S1). The CM14 model in which CTRL is embedded has also been validated against in situ and satellite observations in other portions of the Patagonian shelf (Combes & Matano, 2014a, 2014b, 2019; Matano et al., 2014; Strub et al., 2015).

3.1.2. Seasonal Variability

Volume transport around BB varies substantially seasonally and intraseasonally, with minima at the end of summer and spring and maxima during the fall and winter (Figure 2b). Cross-isobath intrusions hamper the along-isobath coherence of the transport. The time series at Section C3, for example, has a maximum in April

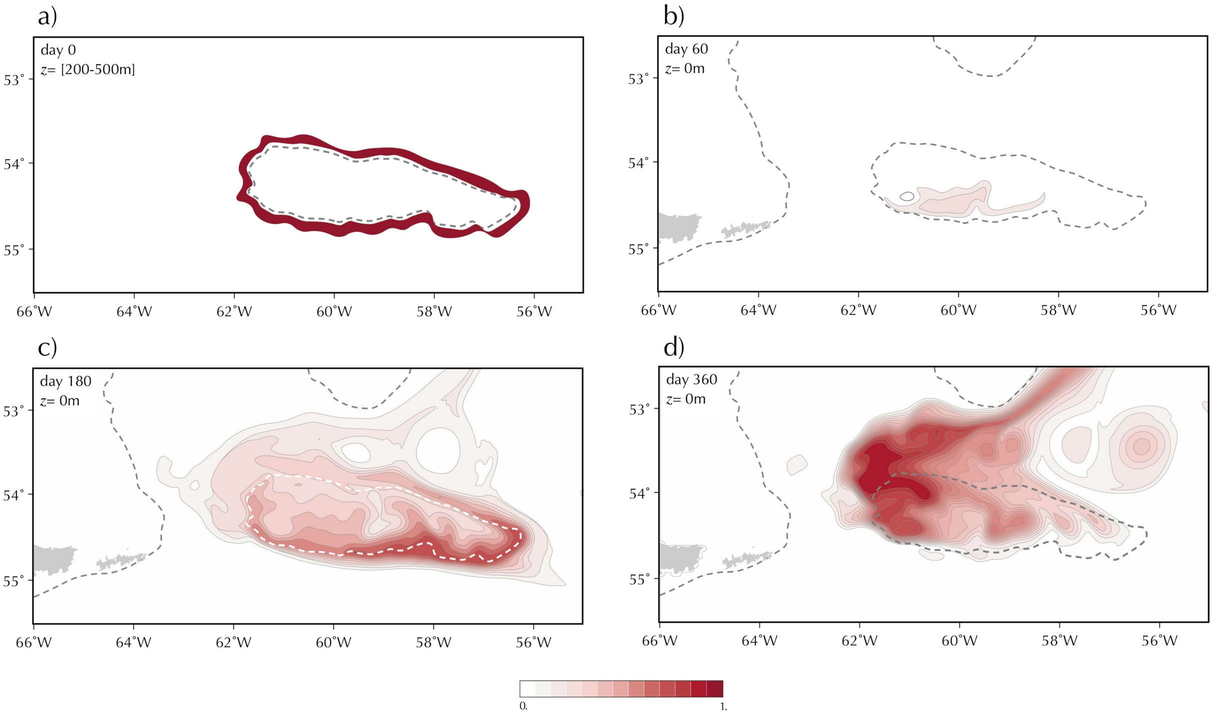

Figure 5. Tracer diagnostic. Snapshots of the time evolution of a passive tracer injected in the deep layers of experiment CTRL. The top left panel shows the initial distribution of the tracer, which is continuously injected (set to 1) between the 200- and 500-m isobaths and below 200 m. The other three panels show *surface* snapshots of the tracer at days 60, 180, and 360.

while C1, which is farther upstream, has a maximum in May (Figure 2b). The amplitude of the transport change at Section C3, moreover, is substantially larger than the one at Section C1, thus revealing that the local April maximum is not significantly influenced by upstream changes. The seasonal change of the Malvinas Current transport close to Section C5 has been extensively discussed in previous studies (Combes & Matano, 2014a, 2014b; Fetter & Matano, 2008; Matano et al., 1993). It is characterized by a minimum during summer and a maximum during fall/winter (Figure 2b). The summer minimum is related to upstream changes in the inshore portion of the ACC, but the fall/winter maximum is not (Figure 2b). Instead, this maximum is driven by changes of the ACC transport farther offshore (Fetter & Matano, 2008).

Temperature and salinity fields show the development of shallow (~50 m) thermocline and halocline during summer and vertical homogenization of the water column during winter (Figure 4). There are no vertical gradients over the portions of the BB that are less than 75 m deep in any season, but instead strong horizontal gradients reflecting the development of Taylor caps on secondary promontories (Figures 3 and 4). These caps encircle regions of warmer, saltier waters during summer, and colder and fresher waters during winter (Figure 4). Model temperature and salinity minima over the bank during winter months are similar to those reported in hydrographic observations (Piola & Gordon, 1989). Vortex trapping of water parcels might contribute to the retention process leading to the modifications of the Antarctic intermediate waters mentioned by Piola and Gordon (1989), whereby winter convection generates cold and fresher waters that later spread into the deep ocean.

3.1.3. Obduction

The BB is a site of intense upwelling and mixing; these processes, which will be collectively referred to as *obduction*, entrain nutrient-rich waters into the photic layer, thus contributing to the fertilization of the surrounding region. The use of the term obduction is prompted by the fact that entrainment of deep waters into the upper layer is not driven by any single dynamical mechanism but by synergetic interaction among them (e.g., upwelling, mixing). In what follows the term *deep waters* refers to waters below 200 m. To document obduction processes we injected a passive tracer around the portion of the BB's slope defined by the 200- and 500-m isobaths and below 200 m (Figure 5a). In this online calculation the tracer is continuously released during a one-year diagnostic integration and its evolution is controlled by an advection/diffusion

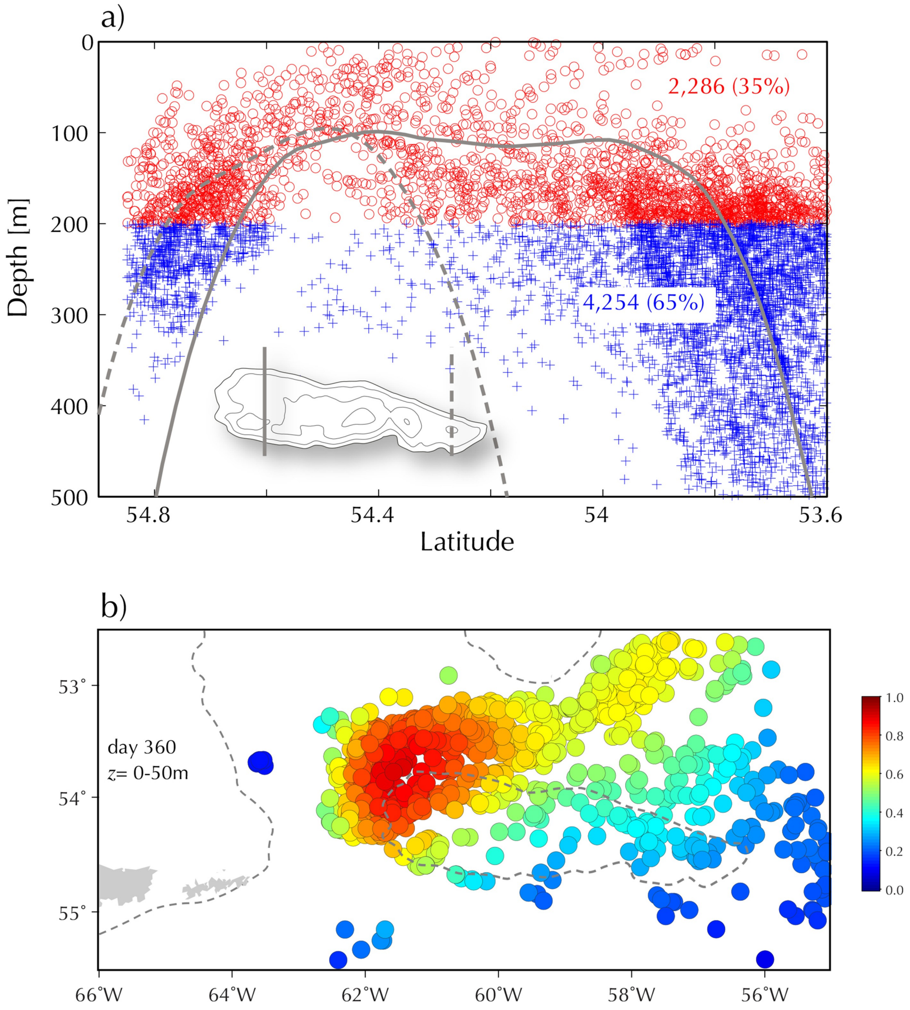

Figure 6. Floats Scatter. Panel (a) shows floats positions in two meridional cross-sections after 120 days of numerical simulation. Floats are released on January 1st at a depth of 200 m. Inset of panel (a) shows the cross-section locations.; (b) float concentration at the surface layer (0–50 m) at the end of the diagnostic integration (day 360).

equation similar to that used for temperature and salinity. After release the tracer is immediately obducted onto shallower layers. At day 60, for example, it forms a surface plume at the southern side of the BB, which is the preferential site for entrainment of open ocean waters into the bank due to the strong cross-isobath flow in that region (Figures 3 and 5b). By day 180 this plume surrounds the bank, with high concentrations around the southern and eastern sides (the preferential obduction sites) and in relatively narrow tongues intruding onto the bank's interior (Figure 5c). At day 360, the tracer accumulates in the northwestern region, which is the main site of detrainment into the open ocean (cf. Figures 3 and 5d).

To quantify the magnitude of the obduction process 6,000 floats, which track water parcel trajectories, are released at 10-day intervals (for a grand total of 216,000 floats at the end of the simulation, day 360) at the same location as the tracer. The particle's trajectories are evaluated during integration time. At day 120, a census of floats released at 200 m shows 35% of the floats above their initial position and 65% below it (Figure 6a). Ancillary analysis shows that time-dependent phenomena (e.g., winter convection, eddies) introduce high-frequency variations to these values. On average, however, 30–40% of the deep waters in the 200–500-m band surrounding the bank are obducted in this region. The two Lagrangian diagnostics, floats and tracer, are consistent. At the end of the simulation (day 360), for example, the concentration of floats in the upper layer (0–50 m) is quite similar to the surface concentration of the passive tracer (cf. Figures 5d and 6b).

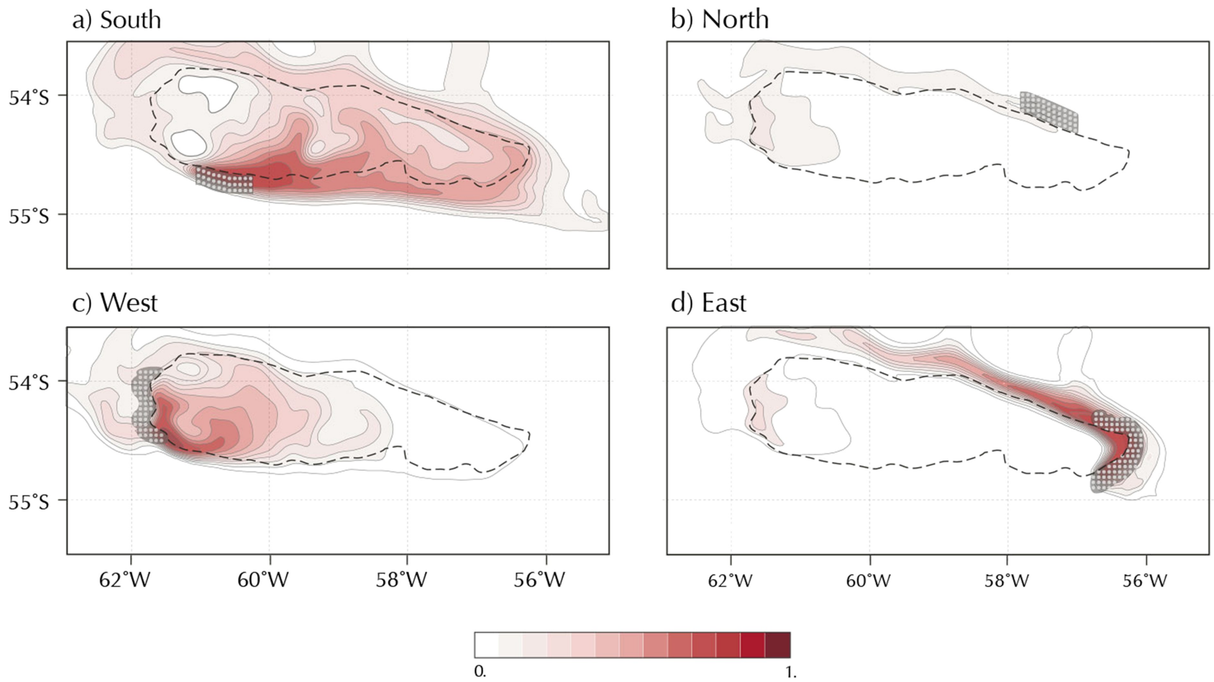

Figure 7. Obduction centers. Surface snapshots at day 180 of the results of different tracer releases. Tracer is continuously injected between the 200- and 500-m isobaths and below 200 m. Stippled areas show the release sites.

The distribution of the tracer over the bank is highly variable because it is constantly modified by tides, wind, eddies, winter convection, etc. This variability can be fully appreciated in Movie S1 which also illustrates the obduction associated with ACC eddies moving along the southern limit of the bank. These eddies, which are frequently generated in the recirculation gyre located at the south side of the bank, can also be observed in animations of satellite SSH data (Movie S2). Tracer obducted in the deep ocean by ACC eddies is advected downstream. Figure 5d, for example, shows the tracer signature of one such eddy located at approximately 56°W, 53.5°S. Most of the tracer carrying eddies are advected around the bank and entrained into the Malvinas Current. Entrainment of eddies into this portion of the Malvinas Current might explain the complex eddy-like features observed in satellite chlorophyll images. The Malvinas Current is not otherwise prone to the development of hydrodynamic instabilities and its trajectory is remarkably stable farther downstream (Matano et al., 2010).

An additional experiment with tracers injected in selected areas around the bank indicates that the main obduction centers are located at the western and southern flanks of the BB (Figure 7). The largest entrainment of obducted waters is observed in the southwestern region (Figures 7a and 7c), which is the location with the strongest cross-isobath flows (Figure 3). There is strong obduction at the eastern side, but most of this tracer is advected around the bank instead of onto it (Figure 7d). The tracer released at the northern site has a very weak surface concentration and, like the previous case, it is advected around the bank and entrained at the southwestern region (Figure 7b). In summary, tracer is mainly entrained along the southwestern side and once onto the bank it is re-circulated and funneled toward the deep ocean in the northwestern region. Inspection of the vertical velocity fields (not shown) shows strong upwelling velocities at the western and southwestern sides of the bank. Upwelling along the western side is favored as it is a stagnation point of the ACC, which bifurcates here into eastward and northward branches, thus creating a region of relatively calm waters (Figure 2a).

Analysis of the tracer balance equation helps to identify the dynamical mechanism contribution to the tracer obduction. If ϕ notes the tracer concentration at each model grid point then its time evolution obeys the equation

$$\frac{\partial\phi}{\partial t}+u\frac{\partial\phi}{\partial x}+v\frac{\partial\phi}{\partial y}+w\frac{\partial\phi}{\partial z}=\frac{\partial}{\partial z}\left(k_z\frac{\partial\phi}{\partial z}\right) \tag{1}$$

where u, v, and w are the two horizontal and vertical components of the velocity field and k_z is the vertical

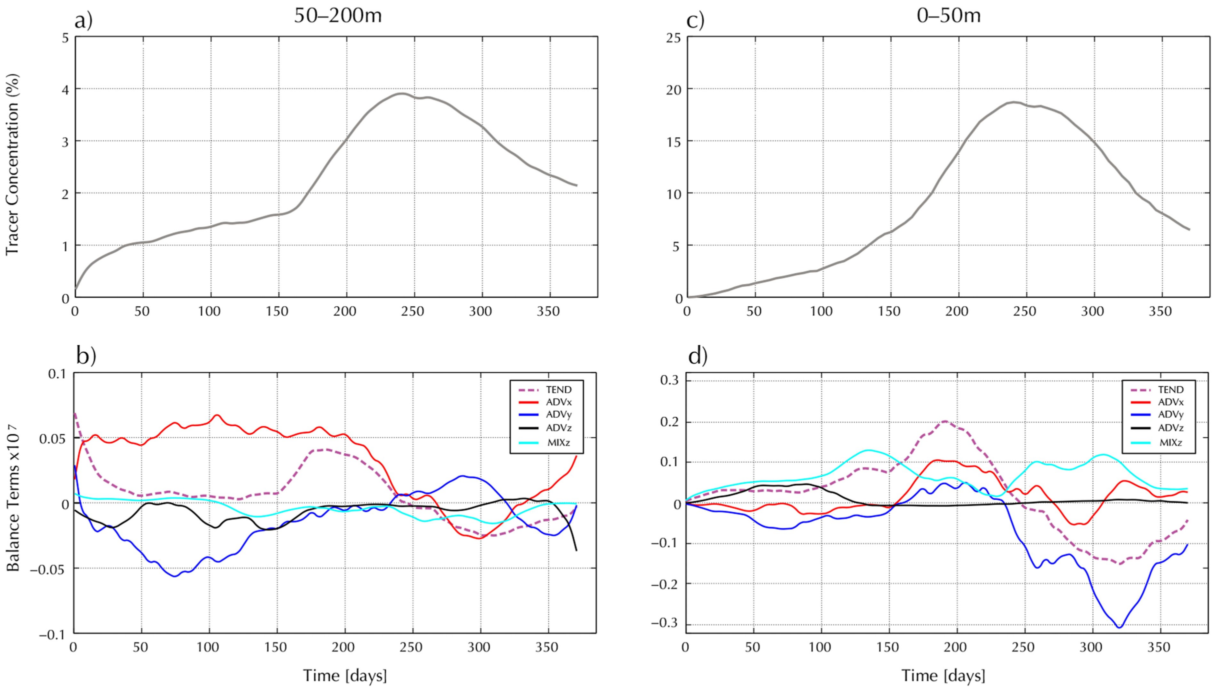

Figure 8. Tracer evolution over the BB summit. Top panels show the time evolution of the area-averaged tracer concentration. Tracer is injected between the 200- and 500-m isobaths and below 200 m: (a) 50 m to bottom and (c) 0–50 m. Bottom panels show the time evolution of the different terms of the tracer balance equation: (b) 50 m to bottom and (d) 0–50 m.

mixing coefficient. In what follows, the terms of equation (1) will be called (from left to right) TEND, ADVx, ADVy, ADVz, and MIXz.

To simplify the analysis each term of equation (1) was vertically averaged in a surface (0–50 m) and deep layer (50–200 m) over the summit (the portion of the bank with depths smaller than 200 m; Figure 8). Tracer development in the deep layer—where obduction begins—shows three well-defined phases: a steady increase during summer and fall (days 1–120), a rapid growth during winter (days 150–220), and a slow decay toward the summer (Figure 8a). These phases are created by seasonal changes in density stratification. Obduction during the first quarter of the year generates a steady supply of tracer to the upper ocean. Convective overturning during winter accelerates this process, leading to a steep growth of the tracer concentration (Figure 8a). Density re-stratification during spring resets the system and the excess tracer of the upper layer is evacuated by the Ekman flow. During this season vertical mixing moves tracer toward the surface where the bank's circulation, which is largely dominated by Ekman transport (ADVy), evacuates the tracer from the bank (Figure 8d). Since there are no tracer sources over the bank, the deep layer concentration changes (TEND) are mostly driven by horizontal advection (Figure 8b). During the first days of the experiment, when there is no tracer over the summit, meridional advection (ADVy) is the dominant entrainment mechanism. After that, the tracer balance reflects the characteristics of the horizontal circulation, which is dominated by predominantly zonal flows in the southern rim of the bank—the preferential entrainment region—and flows with a stronger meridional component in the northern rim—the detrainment region (Figure 3). The steep growth of tracer concentration during winter is driven by convection, which causes an exponential growth of the vertical mixing. This process is not captured in the tracer balance because the increment of tracer concentration over the bank's summit is dominated by lateral advection from the offshore source region.

Variations of tracer concentration in the upper layer are qualitatively similar to those below (Figure 8c). These variations, however, are controlled by different dynamical mechanisms (Figure 8d). Vertical mixing is a fundamental mechanism for the replenishment of tracer in the upper layer of the bank. The vertical mixing coefficient has values of 2×10^{-2} m^2/s during all seasons except winter when it increases by an order of magnitude. Maximum vertical mixing is observed in the western side of the bank, over the region of largest tidal dissipation (Figure S2). The magnitude of the vertical mixing coefficient peaks during winter but MIXz

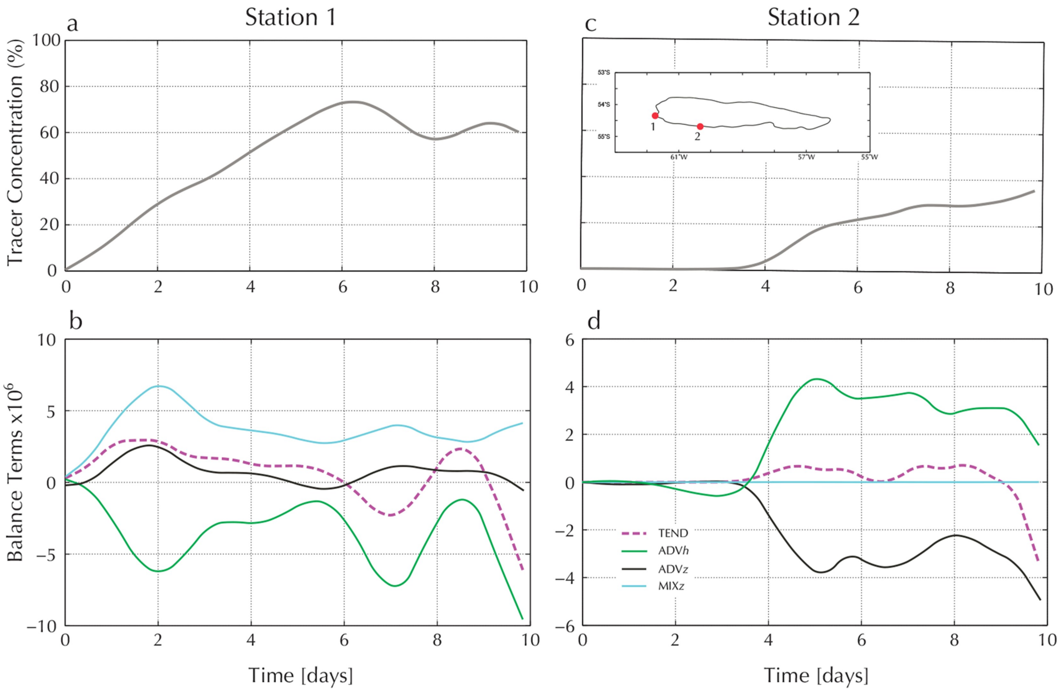

Figure 9. Tracer evolution over the slope region. Top panels show the time evolution of the tracer concentration at two locations around the BB. Bottom panels show the time evolution of the different terms of the tracer balance equation at 100 m. Stations locations are shown in the inset of panel (c).

dips during those months (Figure 8d), thus reducing the tracer flux divergence due to vertical mixing. Upwelling (ADVz) contributes to tracer growth during summer and fall while zonal advection (ADVx) is the most important driver of the winter peak in tracer concentration. ADVz has opposite signs in the deep and upper layers; thus, the same upwelling process that detrains tracer of the deep layer entrains it in the upper layer. A qualitative difference between upper and deep layers is that remote effects (lateral advection) control the tracer evolution of the latter during the entire year, while local effects (vertical mixing) have a larger influence on the former, particularly during summer and fall. During winter and spring lateral advection becomes more important to the tracer balance of both layers. The rapid decay of the tracer in the upper layer during spring is brought by the intensification of meridional advection ADVy, which evacuates the tracer excess accumulated during winter (Figure 8d).

To characterize the evolution of the tracer in the offshore region we mapped the tracer balance equation at the 100-m level, which sits between the surface and the upper limit of the source (200 m), and at two distinct locations: Station 1 and Station 2 (Figure 9). Station 1 typifies obduction in regions with strong tidal dissipation and hence strong mixing and upwelling. Station 2, which is located farther downstream, typifies the tracer evolution in regions controlled by horizontal advection from upstream sources. The analysis focuses on the first 10 days of the experiment (using averages over two M_2 periods). To further simplify the discussion, we grouped ADVx and ADVy in the variable ADVh.

The tracer balance shows that obduction at Station 1 is initially controlled by vertical mixing (MIXz), with a smaller contribution from upwelling (ADVz; Figures 9a and 9b). These processes inject tracer from below, thus increasing its concentration, while ADVh advects it downstream, thus decreasing the local concentration. By day 6 tracer variations at this site are controlled by horizontal advection of tracer obducted at upstream locations (cf. TEND and ADVh). Tracer evolution at Station 2 begins at day 4 and is dominated by a balance between ADVh, which brings tracer from upstream sites and ADVz, which decreases tracer concentrations (Figures 9c and 9d). Obduction at this location is very weak and tracer emergence is dictated by the arrival of the plume generated at Station 1. Tracer evolutions at other locations around are variations of the balances just discussed. Although obduction occurs almost everywhere, after a short period local events are masked by advection from upstream sites. Tracer concentrations, therefore, are susceptible to the

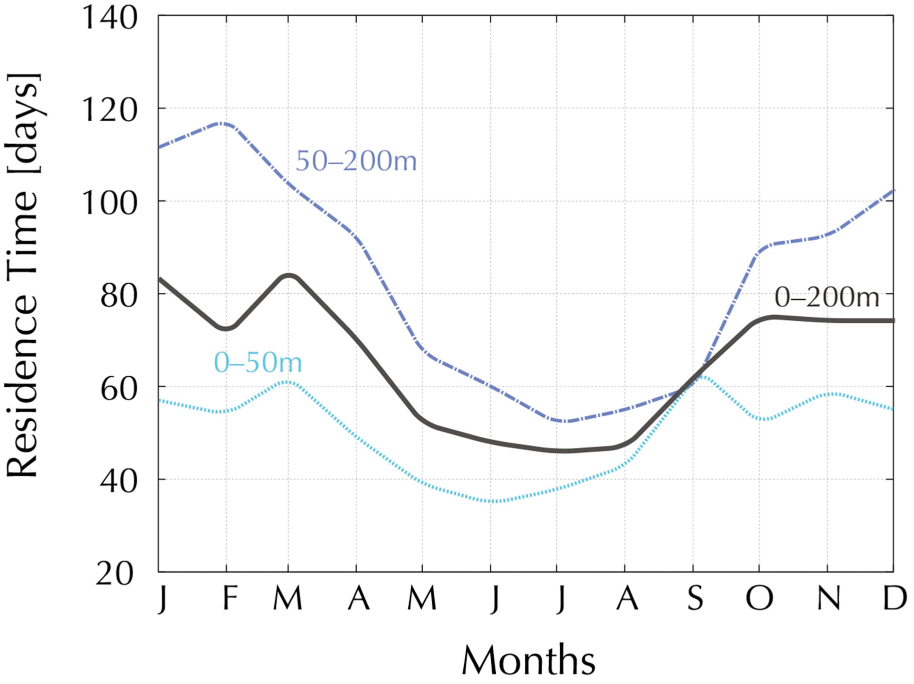

Figure 10. Residence Times. These are defined as the time it takes to evacuate 63% of the floats (e-folding time) from the BB summit (h < 200 m). Release depths: 0–50 m (light blue dotted line), 50–200 m (dark blue dash-dotted line), and 0–200 m (continuous black line).

variability of the local circulation. A Reynolds' decomposition of the tracer balance equation—monthly time mean and five-day anomalies—indicates that, on average, eddy processes drive approximately 5–10% of the tracer variability (Figure S3).

A three-year extension of the tracer diagnostic shows that, after the first winter convection, the tracer evolution follows a remarkable stable cycle characterized by minimum concentration during summer and maximum during winter. There is no year-to-year tracer accumulation over the bank (Figure S4).

3.1.4. Residence Times

Particle tracking is used to estimate the time spent by water parcels over the BB summit ($h < 200$ m). During the last year of the CTRL experiment we released 32,000 floats/month. At the initial state these floats were uniformly distributed between 10 m and the bottom. Residence time is defined as the time it takes to evacuate 63% of the floats (*e*-folding time) from the BB. To evaluate depth dependence, the floats are divided into two groups: upper (0–50 m) and deep (50–200 m), with membership dictated by the initial position of the floats.

The overall residence time (all the floats) is characterized by a minimum during winter (49 days) and a maximum during summer (83 days; Figure 10). Similar seasonal variations are observed for particles released in the upper and deep layers. Seasonal changes in the former, however, are substantially smaller than in the later. Maximum/minimum residence times are around 60/35 days in the upper layer and 115/55 days in the deep layer. Changes of stratification are the main drivers of these seasonal variations since the local wind stress is relatively steady (Figure S5). Tidal mixing during summer generates a relatively strong density front between the bank and the deep ocean (Figure 4). The thermal-wind balance generated by this front intensifies the along-isobath flow (cf. Figures S6a and S6b), thus strengthening the retention of floats inside the bank (Figures S6c and S6d). Density-enhanced trapping over the interior seamounts further strengthens the float retention, thus leading to longer residence times in the deep layers (Figure 10). Chen et al. (1995) described a similar trapping mechanism in their numerical study of the Georges Bank's circulation. During winter erosion of the cross-bank density gradient weakens the along-isobath flow in the upper layer (Figures S6e–S6h). This weakening facilitates the cross-bank exchanges, thus reducing the differences of residence times between upper and deeper layers, which, by the end of winter, are nearly identical (Figure 10). Re-stratification during spring increases the residence times. These increments are steeper on the deep layer on account of the strengthening of bottom trapping associated with tidal mixing.

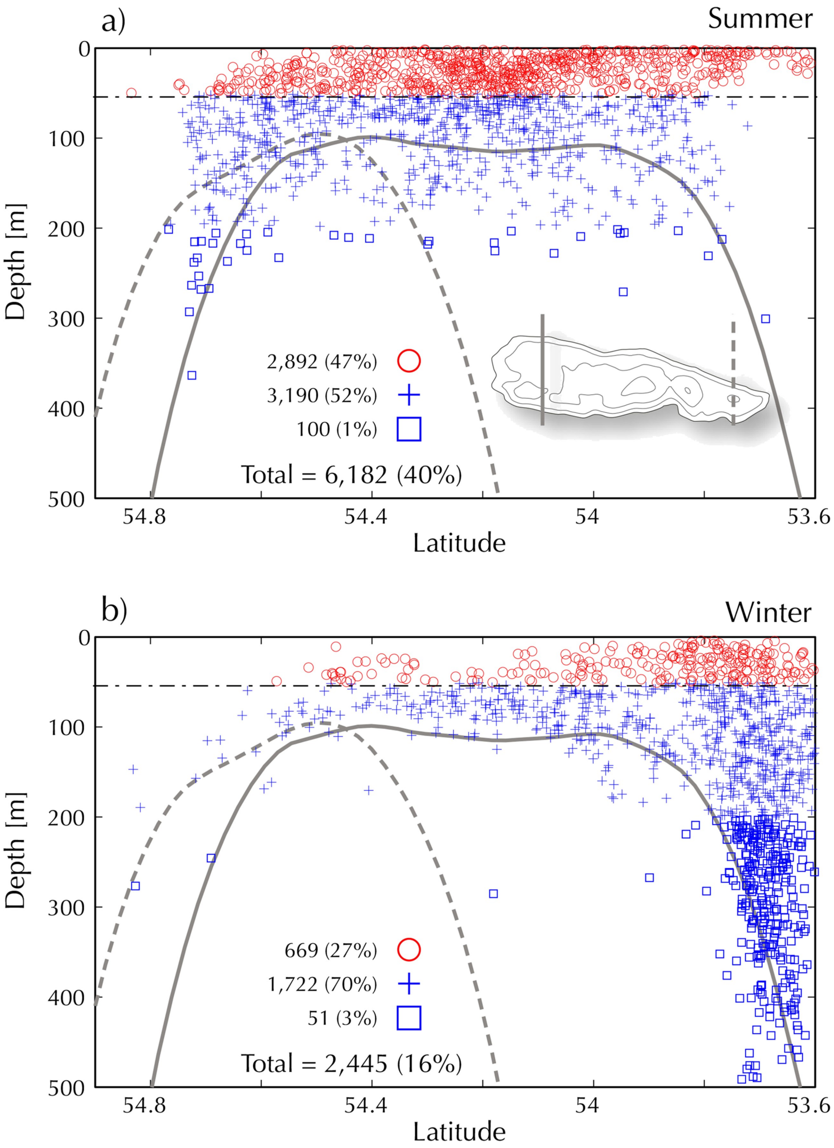

Figure 11. Floats Scattering. Meridional cross-sections showing the positions of floats released in the surface layer (h < 50m depth). Sampling was done after 60 days of numerical simulation. Red circles represents floats that remained above 50 m, blue crosses those that moved downward (50 to 200 m), and blue squares floats that moved below 200 m. The inset of panel (a) shows the locations of the two cross-sections.

Grouping of floats according their initial location is a convenient way to characterize upper and deeper level residence times (Figure 10). Floats, however, do not remain in their initial level but move up and down the water column, thus changing the dynamical mechanisms controlling their residence times. To quantify these displacements, we did scatterplots of 15,000 floats released in the upper level ($h < 50$ m) at the beginning of January (summer) and July (winter) and surveyed after 60 days of numerical simulation (Figure 11). The summer plot shows 6,182 floats (40%) over the BB region. Although all floats were initially located above 50 m, 53% moved below that depth at the time of the survey. Floats in the upper layers were more rapidly detrained from the region than those below, thus leaving a skewed distribution. A more skewed distribution is found in the winter, when only 27% of the remaining floats are located in the upper layer. Winter convection favors not only a more rapid detrainment of floats—the number of remaining floats has been reduced to 2,445 (16%)—but also a larger subduction. In fact, 73% of the floats are now below their initial depth. Note that a relatively small amount of floats (3%; square symbols) are now located below 200 m, some reaching as deep as 500 m. These floats positions suggest formation of denser waters over the bank (e.g., Piola & Gordon, 1989). Analysis of this process is beyond the scope of this study.

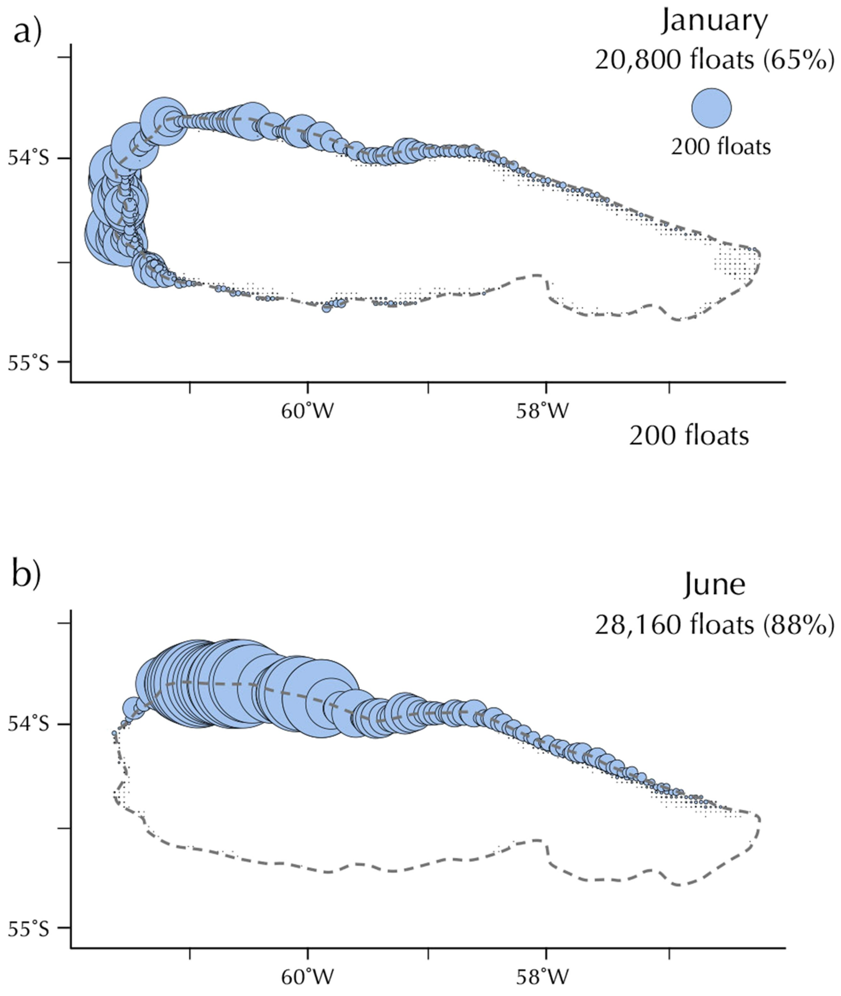

Figure 12. Detrainment sites. Geographical census of preferred location of floats detrainment sites. Radii of circles are proportional to the number of floats leaving the BB at that location: (a) January and (b) June. 32,000 floats are released on top of the BB at the beginning of each month.

A geographic census of the number of floats crossing the 200-m isobath 90 days after release reveals seasonal differences in detrainment locations (Figure 12). The number of floats leaving the bank during summer is substantially smaller than in winter, reflecting the longer residence times reported before (cf. Figures 12a and 12b). During winter, short residence times correspond with larger detrainments (Figure 10). The preferential detrainment site is the northwestern region that extends from the western limit of the 200-m isobath to approximately 60°W, outside of which the number of floats leaving is sharply reduced (Figure 12b). There is no detrainment at the southern side. During summer, the strengthening of the along-isobath flow shifts the preferential detrainment site toward the westernmost tip of the bank (Figure 12a).

3.1.5. Water Sources

To identify the BB water sources, we did an off-line backward time integration of fluid particles using the five-day averaged velocity fields from the CM14 model, which encompasses a larger domain (Figure 1). For this calculation 227,520 floats were released on the bank's summit ($10 \leq z \leq 200$ m) every 10 m and during a one-year period (18,960 particles/month). To facilitate the visualization, we only show 2,000 trajectories (less than 1%) at the end of the study (Figure 13). All trajectories originate in the Pacific Basin and are advected onto the BB by the ACC. The main water sources are the two northernmost jets of the ACC, although particles can be traced as far south as 62°S. A census at the end of the one-year integration shows 198,358 particles (87%) crossing the 74°W longitude line. Of those 60,031 particles are between 0 and 50 m, 70,677 between 50 and 200 m, and 67,650 between 200 m and the bottom. Thus, only 30% of the waters entrained on the BB had a surface origin: the remaining 70% is mainly obducted at the bank or in transit to

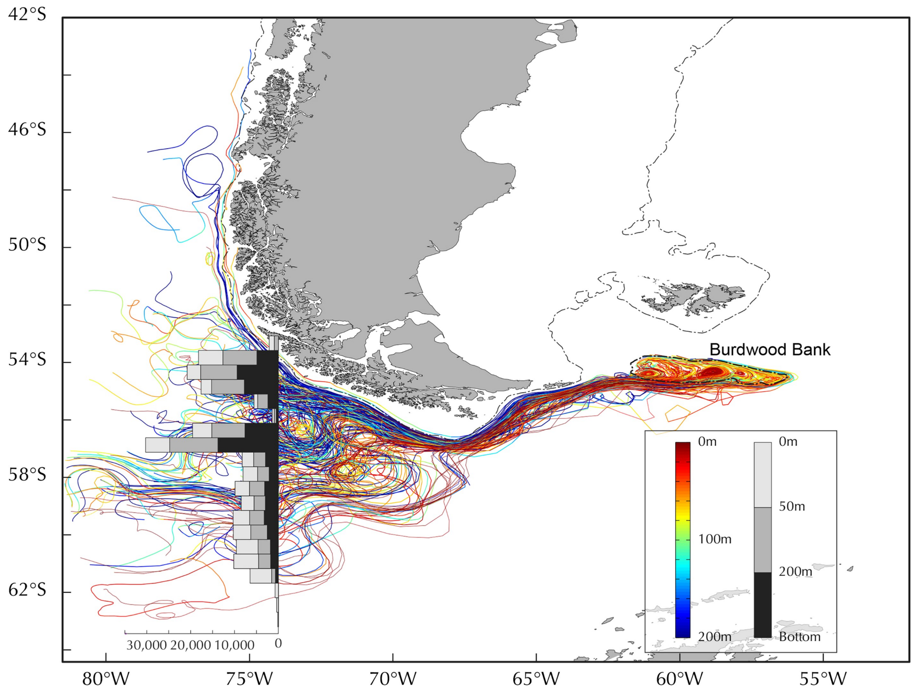

Figure 13. BB water sources. Backward integration of the trajectories of 227,520 floats released over the top of the BB summit during a one-year period (18,960 particles/month). These trajectories are calculated from the 3DWIND velocity field. For the sake of clarity this figure only shows 2,000 of those trajectories (less than 1%). Colors represent depth location of the particles during their journey toward the BB. Histogram represents number and depth of particles at 74°W.

it. The contribution of deep waters brought by the northernmost jet, which is partially fed by the Cape Horn Current, points to a potential connection between marine ecosystems along the Chilean and Argentinean coasts. A smaller number of trajectories (not shown in Figure 13) connect the coastal waters of the Chilean coast with the BB.

3.2. Process-Oriented Experiments

To identify the contributions of different drivers on the BB circulation we did a suite of process-oriented experiments using barotropic and baroclinic versions of the model (Table 1). Barotropic experiments, which are initialized with constant values of temperature and salinity, aim to facilitate the interpretation of the dynamical structures generated in more complex setups. Three barotropic experiments are discussed: TIDES_ONLY, which is only forced at the open boundaries with the M_2 tidal harmonic; WINDS_ONLY, which is only forced with monthly mean winds; and TIDES&WINDS, which is forced with the M_2 tidal harmonic and monthly mean winds. None of these experiments includes the ACC. In addition to CTRL six other experiments include density stratification. The first experiment,STRAT*z*, is initialized with a density field that only varies with depth, that is, $\rho = \rho(z)$. To construct the new density field we horizontally averaged the summer and winter temperature and salinity fields over the BB region. STRAT*z* is only forced with the M_2 tidal harmonic. Barotropic experiments and STRATz are spun up during 90 days, and their analysis is based on the monthly mean of the last 30 days of integration. The other five experiments are initialized as CTRL, but differ in their boundary forcing: ACC_ONLY has no wind or tidal forcing, ACC&TIDES includes tidal forcing but has no wind forcing, ACC&WIND includes wind forcing but has no tidal forcing, 3DWND is similar to CTRL but it is forced with three-day average winds instead of monthly mean winds, and TRCD is also similar to CTRL but its BB is truncated at 200 m. These experiments are spun up to dynamical equilibrium and integrated over five years. The results discussed here are based on the analysis of the last year of model integration.

TIDES_ONLY addresses the impact of tidal forcing on the BB circulation (Figure 14a). The M_2 harmonic, which is the main tidal component in this region, rotates cyclonically around an amphidromic point located south of the Malvinas Islands (Figure S2a). Its propagation is accompanied by an increase of amplitude,

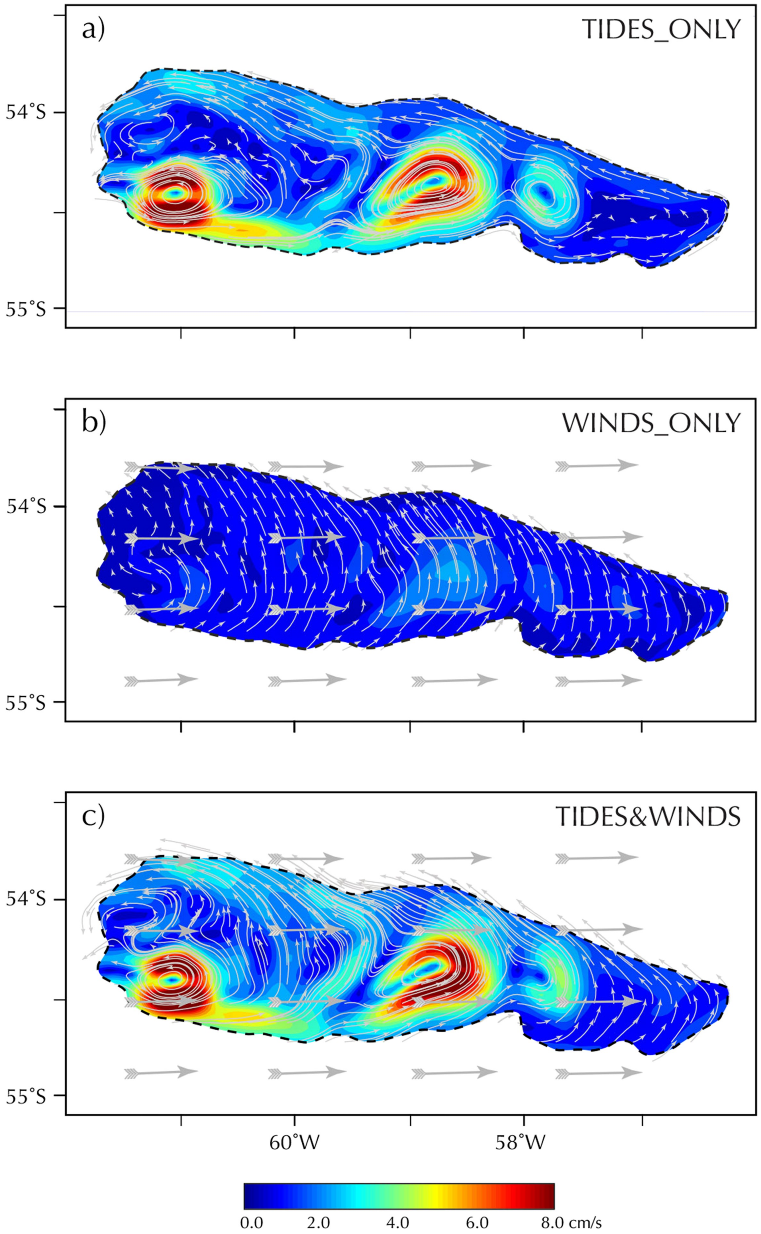

Figure 14. Barotropic sensitivity experiments. Time-mean, depth-averaged velocities of barotropic experiments forced with (a) M_2 tide (TIDES_ONLY), (b) winds (WINDS_ONLY), and (c) winds and M_2 tide (TIDES&WINDS). Colors represent speeds (cm/s). Gray arrows on top of (b) and (c) represent wind stress. Maximum wind magnitude is ~0.1 N/m^2.

which reaches values of ~4 m over the Patagonian shelf (Palma et al., 2004). Tidal amplitudes over the BB are substantially smaller, reaching maximum values of 40 cm and maximum speeds of 60 cm/s. The southwestern region has the largest tidal ellipses and energy fluxes, reaching values of 2×10^5 W/m (Figures S2b and S2c). Tidal dissipation peaks on top of the interior seamounts, with an absolute maximum over the seamount located in the southwestern region (Figure S2c). The tidal energy flux is directed in the cross-isobath direction (NW), thus favoring the nonlinear generation of residual currents. The residual tidal circulation, which generates a transport of ~0.5 Sv around the bank, is characterized by the formation of a bank-wide anticyclonic gyre composed of four to five smaller subgyres rotating around the underlying seamounts (Figure 14a). As expected, this flow has a quite homogeneous vertical structure (Figure S7a).

Tidal forcing generates secondary cross-bank circulation cells, which have strong upwelling/downwelling motions (Figure 15a). These cells are most intense in the southwestern region, where tidal dissipation is

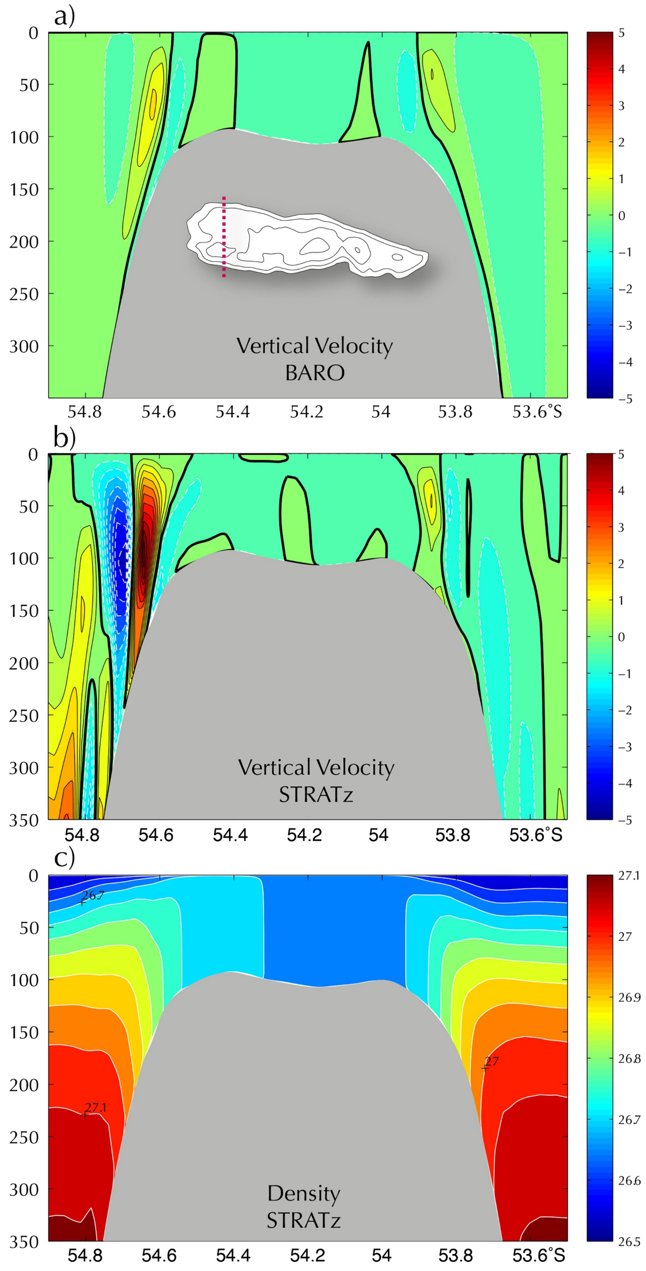

Figure 15. Tidal driven secondary circulation cells. (a) Vertical velocities along a meridional cross section shown in the inset for experiment TIDES_ONLY. (b) Idem for STRAT*z*. (c) Density profile in STRAT*z*. These cross sections represent 30-day averages. Vertical velocities are in units of 10^{-4} m/s.

strongest. Chen and Beardsley (1995) and Chen et al. (1995) described similar cells in the Georges Bank (Gulf of Maine), observing that density stratification intensifies the residual flow. This effect is clearly manifested in experiment STRAT*z* (Figures 15b and 15c). Tidal mixing homogenizes the density structure over the shallow portion of the bank, thus generating a density front that, through thermal wind balance, enhances the tidally rectified flow. Vertical velocities increase from a maximum of 1.4×10^{-4} m/s in TIDES_ONLY to 5.5×10^{-4} m/s in STRATz. An additional STRATz experiment initialized with a winter density profile (not shown) generates weaker tidal front and smaller vertical velocities (3.5×10^{-4} m/s). Tidal interaction with the background density field, nevertheless, still has an important impact on the residual circulation.

The circulation patterns produced by WINDS_ONLY, a barotropic experiment that aims to characterize the contribution of local (over the bank) wind forcing, are consistent with those expected from linear Ekman dynamics, that is, a general northwestward flow constrained to the uppermost layer (top 20m) (Figures 14b and S7b). The model circulation patterns also show the influence bottom topography, which allows the development of barotropic pressure gradients and hence geostrophic balanced flows. At steady state, the momentum balance (not shown) is dominated by Ekman dynamics at the surface and geostrophic balance deep below. Geostrophic velocities are much smaller than Ekman velocities but control the vertically integrated transport in the deep portions of the basin. Over relatively shallow regions like the BB summit, however, the Ekman flow is the dominant feature of the local circulation, which is characterized by a broad northward flow over the bank and a counterclockwise current around its flanks (Figure 14b). The dominance of the Ekman dynamics is reflected in the lack of vortices over the interior seamounts.

TIDES&WINDS is roughly a linear combination of the previous results (Figure 14c). Circulation patterns are similar to those of TIDES_ONLY with two important exceptions. First, the depth-averaged flow is more intense, particularly in relatively deep regions (Figure S7c). Second, there is a substantial increase in cross-bank flows. In the TIDES_ONLY case most of the entrainment of deep-ocean waters is restricted to the southwestern portion of the bank while most of the detrainment lay on the western margin. In TIDES&WINDS, however, there are relatively large entrainments all along the southern boundary of the bank and the large detrainments have shifted toward its northwestern side (Figure 14c). The velocity shows a stronger vertical shear than TIDES_ONLY, which is associated with the wind-driven intensification of the circulation in the surface layer (cf. Figures S7a and S7c).

Barotropic experiments suggest that tides are a dominant driver of the BB circulation, having a larger influence than local winds (cf. Figures 3 and 14). This dominance is important to the bank's ecosystem because tidal forcing intensifies secondary recirculation cells, thus creating convoluted circulation paths that increase the retention of fluid parcels. Wind forcing, however, generates a meridional Ekman flow that short-circuits the trajectory of fluid parcels, thus shortening residence times. Barotropic experiments also suggest that while tides generate preferential paths for the exchanges between the bank and the deep ocean wind forcing does not. Cross-bank exchanges in TIDES_ONLY are largely confined to a relatively small portion of the western sector of the bank (Figure 14a). In WINDS_ONLY these exchanges extend all along the summit's rim (Figure 14b). CTRL and TIDES_ONLY reveal almost identical entrainment/detrainment sites, which also suggests that tidally rectified currents play an important role in the communication between the BB and the deep ocean. The relative contribution of tides and winds to BB

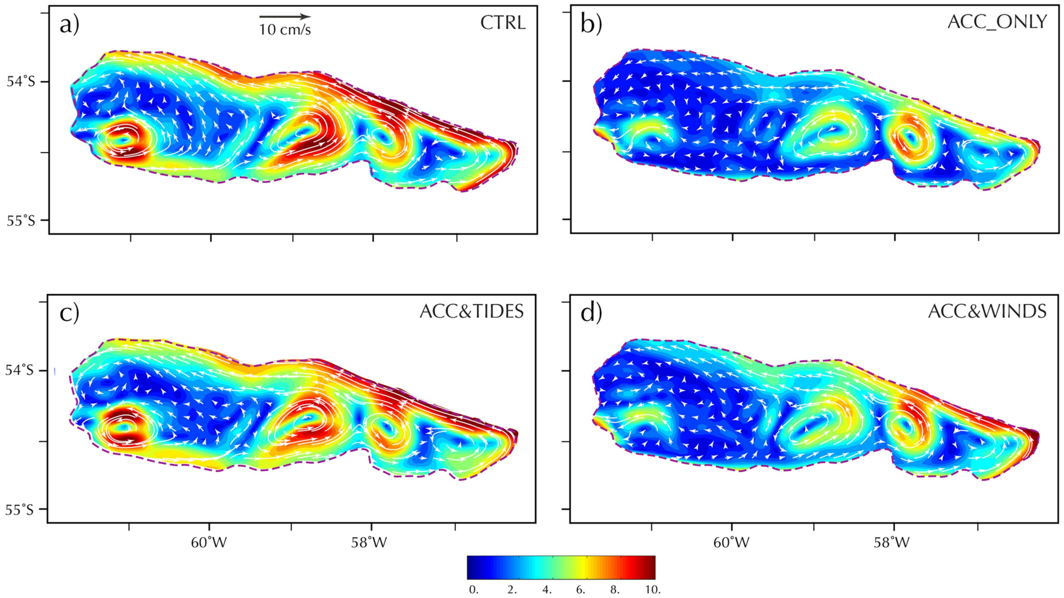

Figure 16. Baroclinic sensitivity experiments. Time-mean depth-averaged velocities of the baroclinic experiments forced with (a) CTRL, (b) ACC only, (c) ACC and M_2 tide, and (d) ACC and winds. All sensitivity experiments (b–d) are initialized as CTRL and run until dynamical equilibrium. Background colors represent flow speeds (cm/s).

circulation is further explored in the following section, where the contributions of density stratification and the ACC are included.

The results of the baroclinic experiments are qualitatively similar to the barotropic suite, thus demonstrating their robustness (Figure 16). They also confirm the preliminary conclusion that tides are the main driving mechanism. Differences between experiments are not qualitative but quantitative; barotropic and baroclinic experiments differ in the magnitude of the velocities but not in the direction of the flow. Some of the results of the baroclinic experiments deserve clarification. It seems counterintuitive, for example, that ACC_ONLY

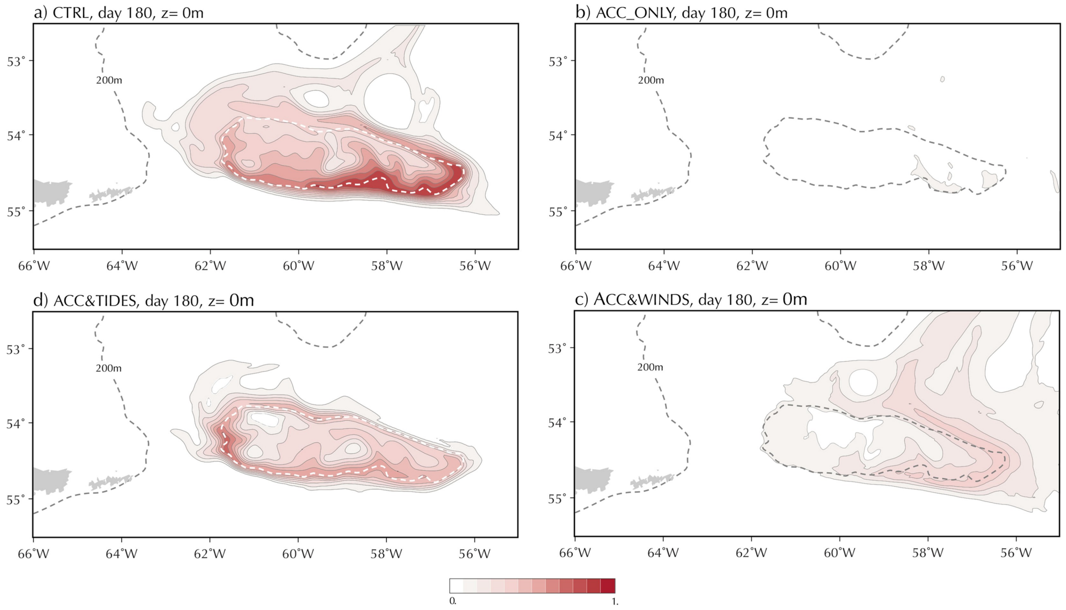

Figure 17. Obduction Sensitivity. Surface snapshots at day 180 of tracer releases in the baroclinic sensitivity experiments. This diagnostic aims to identify the main obduction processes. Tracer is continuously injected between the 200m and 500m isobaths and below 200 m.

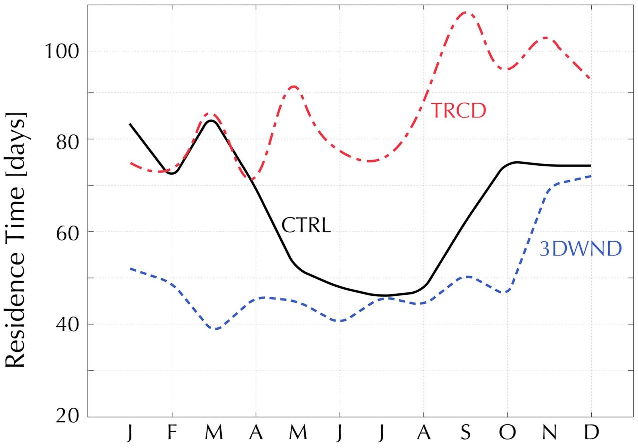

Figure 18. Retention times sensitivity. Comparison of the seasonal variations of retention times in experiments CTRL (red dotted line), 3DWIND (blue dashed line), and TRCD (red dash-dotted line).

shows the largest velocities in the interior of the bank and not on its southern flank, where the ACC is stronger. Two facts explain this feature. First, the large velocities on top of seamounts are associated with the shallow depths of these regions (Figure 16 shows depth-averaged velocities). Second, in the absence of local wind forcing, weak stratification favors a shift of the ACC toward deeper waters, thus weakening its impact on the bank's circulation. The dominant influence of tidal forcing on the bank's circulation is clearly evident in the comparison between CTRL and ACC&TIDES and ACC&WINDS.

Tracers injected in the sensitivity experiments illustrate the importance of the different driving mechanisms to the obduction process (Figure 17). Experiment ACC_ONLY shows that, even in the absence of tidal and (local) wind forcing, the ACC is able to obduct deep waters, albeit a very small amount, which manifests in the southeastern corner of the bank (Figure 17b). It is beyond the scope of this article to make an exhaustive analysis of the mechanisms driving upwelling, but the characteristics of the flow around the bank's southern rim, namely, weak stratification and cyclonic circulation, suggest that it is driven by topographic effects. Previous studies have shown that the lateral spreading of a barotropic equivalent current, like the ACC, is inversely proportional to the slope of the bottom (Csanady, 1978; Hill, 1995). Thus, abrupt changes of bottom slope generate divergences of the horizontal flow and, as a consequence, upwelling (Matano & Palma, 2008; Miller et al., 2011). Inclusion of local wind forcing, in experiment ACC&WINDS strengthens this upwelling significantly, which now extends all along the bank's perimeter (Figure 17c). This strengthening is a response to the synergetic interaction between local wind forcing and the ACC. In this particular case, local wind forcing contributes to further uplift deep waters that have been already upwelled by the interaction between the ACC and the bottom topography. Experiment ACC&TIDES shows the largest surface tracer concentrations of the three sensitivity experiments, further demonstrating the importance of tidal forcing on the tracer obduction (Figure 17d). Maximum tracer values are observed in the southwestern limit of the bank (Figure 17d) where tidal dissipation is largest (Figure S2c). The tracer concentration in CTRL is larger than in any of the individual sensitivity experiments, indicating a synergistic interaction among the different obduction mechanisms (Figure 17a).

Experiments 3DWND and TRCD test the sensitivity of residence times to atmospheric forcing and bottom topography. The 3DWND is identical to CTRL except that is forced with three-day averaged winds (instead of monthly mean winds). This integration was initialized with the year 4 of CTRL and run for one additional year (2016). The 3DWND residence times are shorter than CTRL (Figure 18). Differences are larger during summer, when CTRL estimates are nearly twice as large as 3DWND's. This difference reflects the stronger-than-average winds during summer of 2016 (Figure S5). Dependence of residence times on wind conditions also manifests in the closeness between the 3DWND and CTRL residence times during November and December, when local wind conditions are close to the climatological values (Figure S5). The impact of local wind forcing on residence times is modulated by density stratification. During the winter of 2016 winds departed significantly from the climatology, yet residence time remained close, suggesting that when vertical mixing is strong, variations in the local wind intensity have little impact on the residence times. Variability of the ACC transport has no significant influence on residence times. Findings from an ancillary experiment in which the ACC transport is fixed to its climatological value are nearly identical to those for year 2016. The sensitivity experiments illustrate how variable, and dependent on the local wind conditions, residence times can be. Present analysis, moreover, suggests that local wind forcing is the main mechanism for the detrainment of water parcels from the BB.

In experiment TRCD the top of the BB has been shaved to 200-m depth to evaluate the sensitivity of retention times to irregularities of BB topography. Comparison of retention times in CTRL and TRCD shows shorter times in the former (Figure 18). Differences, which increase from approximately 20 days at the upper level to 30 days at the bottom level, reflect the impact of bottom topography on the bank's circulation. January surface and bottom circulation patterns illustrate the differences between CTRL and TRCD (Figure 19). Circulation in CTRL is dominated by seamount-induced vortices that contribute to the retention of fluid parcels and funnel the cross-bank circulation toward the northwest (Figures 19a and 19c). TRCD, however, shows little influence of the underlying bottom on the upper level circulation, which, in contrast to the CTRL, is directed toward the northeast, that is, in the opposite direction of the bottom flow (Figures 19b and 19d). Bottom topography affects not only retention times but also the preferential detrainment sites, which shift to the southwest (Figures 19e and 19f).

Experiment TRCD shows that changes of the summit configuration produce substantial changes of the BB circulation but retention times still remain relatively large. Summit topography has a larger impact on the obduction of deep waters, which is substantially weakened (Figure S8). The deepening of the bank ameliorates the impact of tidal mixing on the obduction of deep waters, thus weakening the surface concentration of the tracer. To further estimate the impact of mixing on residence times we released 24,500 floats, which were located between 50 and 200 m, at the beginning of summer (January) and winter (July) and made a census of their location after 60 days of numerical integration. For the summer release we found that only approximately 2.5% of the floats released are entrained into the surface layer (18% for the CTRL case). For the winter release that percentage increased to 12.5% due to enhanced convection (6% for CTRL).

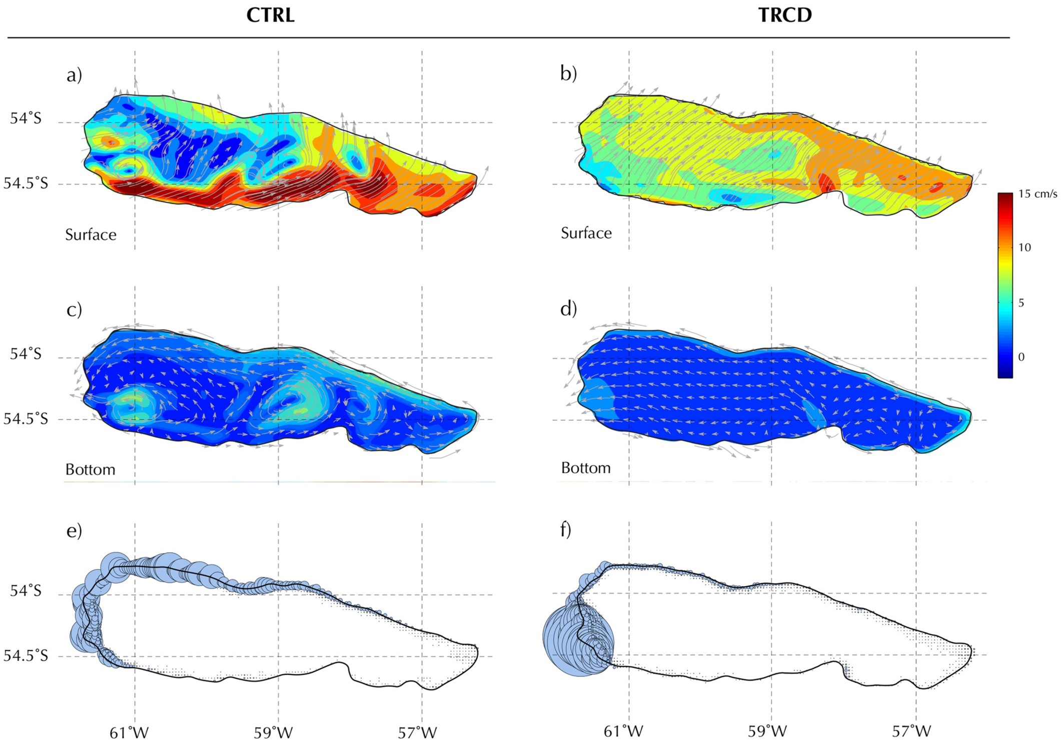

Figure 19. Bottom topography sensitivity. (a–d) Surface and bottom velocities of experiments CTRL and TRCD, in which the BB is leveled at 200 m. (e and f) The result of a geographical census of floats released on top of the summit of both experiments. Background colors in the top two rows represent flow speeds.

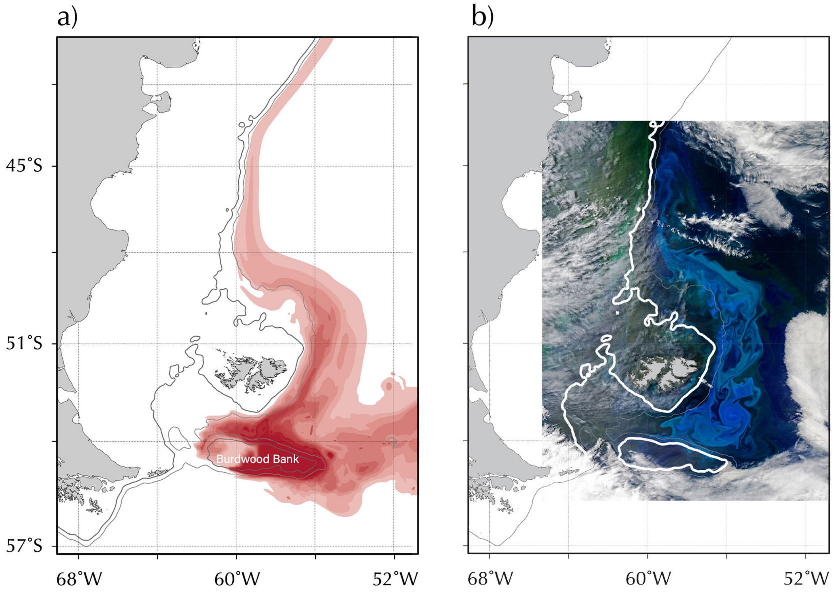

Figure 20. Model and observations. (a) Surface snapshot at day 360 of the CTRL tracer release around the BB. (b) Ocean color snapshot from the Aqua MODIS Landscape Rapid Response Team mission. This image was taken 28 December 2017.

Although experiment TRCD is an extreme modification of the bank's topography, the two main contributions of the BB to the fertilization process, namely, retention and obduction, still persist. In fact, we choose to show a tracer snapshot at day 120 (Figure S8) because by day 180 winter convection had already started to mix the bank waters, thus diluting the differences between CTRL and TRCD. That is, obduction of deep waters over the BB is a robust feature because even though it is strongly modulated by tides, it does not depend on a single physical mechanism.

The condition of no diffusive flux requires that isopycnals be normal to the bottom (Cummins & Foreman, 1998; Phillips, 1970). Thus, even in the absence of external forcing, vertical mixing should lead to a distortion of isopycnals at the bottom that generates an along-slope pressure gradient. According to Cummins and Foreman (1998) such distortions drives bottom intensified ageostrophic flows of considerable magnitude. To evaluate the contribution of bottom mixing to cross-slope flows we did an additional experiment using STRAT*z* initial conditions but without external forcing. The results (not shown) are consistent with those described by Cummins and Foreman (1998). The intensities of the secondary circulation cells produced by bottom mixing, however, are 1 to 2 orders of magnitude smaller than those predicted by them and, also, than those generated in the tidally forced STRAT*z* experiment. The difference is explained by vertical mixing parameterization. Cummins and Foreman (1998) imposed a fixed vertical mixing profile with a maximum diffusivity of 1 cm^2/s at the bottom while in the present experiment the vertical mixing coefficient is determined by the K-Profile Parameterization scheme, which in this particular case produces values that are orders of magnitude smaller.

4. Final Remarks

The present analysis suggests that BB is an active center for the obduction of deep, fertile waters to the surface layers of the Drake Passage. This phenomenon, which includes upwelling and mixing, is primarily driven by tides and strengthened by winter convection. Wind forcing is the main driver for the detrainment of the bank's waters contributing to the obduction process through the enhancement of vertical mixing. Wind forcing, however, is not a major obduction driver, since without the contribution of tidal forcing it would be incapable to uplift waters from 200-m depth. The circulation patterns inferred from the model are robust, as they are generated for different model configurations. In fact, with the exception of the extremely idealized WINDS_ONLY and TRCD cases all the other experiments—barotropic and baroclinic—produce very similar circulation patterns, consisting of a broad anticyclonic flow around the bank's rim and anticyclonic vortices on top of the interior seamounts. There is, however, scant observational evidence to corroborate the model predictions. Most notably, satellite color imagery does not consistently show substantial chlorophyll blooms over the bank, although a recent survey shows high concentrations of small-sized phytoplankton (V. Guinder et al., manuscript in preparation). There are several potential explanations for the absence of significant chlorophyll blooms, including lack of light due to persistent cloud cover, a deep mixed layer, fast ocean currents advecting nutrients to the subpolar basin, the possibility that blooms, while extant, might not develop on the surface but in deeper layers. None of these possibilities can be confirmed at this stage.

The obduction processes documented herein could have a significant impact not only on local ecosystems but also on the biogeochemical balance of the Southern Ocean. The renewal of surface waters over the BB is a continuous phenomenon sustained by the synergistic action of diverse drivers. Our simulations suggest that the deep waters brought to the surface in this region are immediately advected to the Brazil/Malvinas Confluence, where higher stratification, solar radiation, and phytoplankton contents might allow the development of the intense chlorophyll blooms routinely seen in satellite imagery (Garcia et al., 2008; Romero et al., 2006). The tracer plume produced by our most realistic experiment provides the physical framework for this hypothesis (Figure 20a). After being obducted at the BB the waters tagged by this plume are entrained into the Malvinas Currents, whereupon they are advected beyond the Drake Passage and into the Brazil/Malvinas Confluence. Phytoplankton plumes similar to that generated by the model's tracer are frequently seen in satellite color imagery (Figure 20b).

Acknowledgments
We are very grateful for the time and effort invested by two anonymous reviewers and the editor in the improvement of this manuscript. Their kind and thoughtful comments improved substantially this article. R. Matano and V. Combes acknowledge NASA support through grant NNX17AH20G and the National Science Foundation through grants OCE-1559550 and OCE-1830856. E.D. Palma acknowledges financial support from Agencia Nacional de Promoción Científica y Tecnológica (grant PICT16-0557) and Universidad Nacional del Sur (grant 24F066), Argentina. The comments of Jacobo Martin, Yvette Spitz, and Valeria Guinder during the preparation of this article are greatly appreciated. Altimeter data described in this article can be accessed in https://aviso.altimetry.fr/en/data/data-access/ftp.html.

References

Amante, C., & Eakins, B. W. (2009). ETOPO1 1 arc-minute global relief model: Procedures, data sources and analysis. National Geophysical Data Center, NOAA, Boulder Colorado.

Barnier, B. (1998). Forcing the ocean. In E. P. Chassingnet, & J. Verron (Eds.), *Ocean modelling and parameterization* (pp. 45–80). The Netherlands: Kluwer Academic Publishers. https://doi.org/10.1007/978-94-011-5096-5_2

Beckmann, A., & Haidvogel, D. B. (1997). A numerical simulation of flow at Fieberling Guyot. *Journal of Geophysical Research*, *102*(C3), 5595–5613. https://doi.org/10.1029/96JC03414

Beckmann, A., & Mohn, C. (2002). The upper ocean circulation at Great Meteor Seamount. Part II: Retention potential of the seamount-induced circulation. *Ocean Dynamics*, *52*(4), 194–204. https://doi.org/10.1007/s10236-002-0018-3

Beckmann, A., Timmermann, R., Pereira, A. F., & Mohn, C. (2001). The effect of flow at Maud Rise on the sea-ice cover–numerical experiments. *Ocean Dynamics*, *52*(1), 0011–0025. https://doi.org/10.1007/s10236-001-8173-5

Boehlert, G. W., & Genin, A. (1987). A review of the effects of seamounts on biological processes. In *Seamounts, Islands and Atolls* (Vol. 43, pp. 319–334). Washington D. C.: American Geophysical Union.

Brink, K. H. (1989). The effect of stratification on seamount-trapped waves. *Deep Sea Research*, *36*(6), 825–844. https://doi.org/10.1016/0198-0149(89)90031-9

Butman, B., Beardsley, R. C., Magnell, B., Frye, D., Vermersch, J. A., Schlitz, R., & Noble, M. A. (1982). Recent observations of the mean circulation on Georges Bank. *Journal of Physical Oceanography*, *12*(6), 569–591. https://doi.org/10.1175/1520-0485(1982)012<0569:ROOTMC>2.0.CO;2

Chapman, D. C., & Haidvogel, D. B. (1992). Formation of Taylor caps over a tall isolated seamount in a stratified ocean. *Geophysical and Astrophysical Fluid Dynamics*, *64*(1-4), 31–65. https://doi.org/10.1080/03091929208228084

Chen, C., Beardsley, R., & Franks, P. J. S. (2001). A 3-D prognostic numerical model study of the Georges Bank ecosystem. Part I: Physical model. *Deep-Sea Research Part II*, *48*(1-3), 419–456. https://doi.org/10.1016/S0967-0645(00)00124-7

Chen, C., & Beardsley, R. C. (1995). A numerical study of stratified tidal rectification over finite-amplitude banks. Part I: Symmetric banks. *Journal of Physical Oceanography*, *25*(9), 2090–2110. https://doi.org/10.1175/1520-0485(1995)025<2090:ANSOST>2.0.CO;2

Chen, C., & Beardsley, R. C. (1998). Tidal mixing and cross-frontal particle exchange over a finite amplitude asymmetric bank: A model study with application to Georges Bank. *Journal of Marine Research*, *56*(6), 1163–1201. https://doi.org/10.1357/002224098765093607

Chen, C., Beardsley, R. C., & Limeburner, R. (1995). A numerical study of stratified tidal rectification over finite-amplitude banks. Part II: Georges Bank. *Journal of Physical Oceanography*, *25*(9), 2111–2128. https://doi.org/10.1175/1520-0485(1995)025<2111:ANSOST>2.0.CO;2

Combes, V., & Matano, R. P. (2014a). A two-way nested simulation of the oceanic circulation in the sSouthwestern Atlantic. *Journal of Geophysical Research: Oceans*, *119*, 731–756. https://doi.org/10.1002/2013JC009498

Combes, V., & Matano, R. P. (2014b). Trends in the Brazil/Malvinas confluence region. *Geophysical Research Letters*, *41*, 8971–8977. https://doi.org/10.1002/2014GL062523

Combes, V., & Matano, R. P. (2018). The Patagonian shelf circulation: Drivers and variability. *Progress in Oceanography*, *167*, 24–43. https://doi.org/10.1016/j.pocean.2018.07.003

Combes, V. & Matano, R.P. (2019). On the origins of the low-frequency seasurface height variability of the Patagonia shelf region. *Ocean Modelling*, *142*, https://doi.org/10.1016/j.ocemod.2019.101454

Csanady, G. T. (1978). The arrested topographic wave. *Journal of Physical Oceanography*, *8*(1), pp.47–62.

Cummins, P. F., & Foreman, M. G. G. (1998). A numerical study of circulation driven by mixing over a submarine bank. *Deep-Sea Res. Part I*, *45*(4-5), 745–769. https://doi.org/10.1016/S0967-0637(97)00102-7

Da Silva, A. M., Young, C. C., & Levitus, S. (1994). *Atlas of surface marine data 1994, vol. 1, Algorithms and procedures*, *NOAA Atlas NESDIS* (Vol. 8, p. 83). Washington, D.C.: U. S. Dep. of Commer., NOAA, NESDIS.

Egbert, G. D., Bennet, A. F., & Foreman, M. G. G. (1994). TOPEX/Poseidon tides estimated using a global inverse model. *Journal of Geophysical Research*, *99*(C12), 24,821–24,852. https://doi.org/10.1029/94JC01894

Fetter, A. F. H., & Matano, R. P. (2008). On the origins of the variability of the Malvinas Current in a global, eddy permitting numerical simulation. *Journal of Geophysical Research*, *113*, C11018. https://doi.org/10.1029/2008JC004875

Franks, P. J., & Chen, C. (1996). Plankton production in tidal fronts: a A model of Georges Bank in summer. *Journal of Marine Research*, *54*(4), 631–651. https://doi.org/10.1357/0022240963213718

Garcia, V. M. T., Garcia, C. A. E., Mata, M. M., Pollery, M. M. R., Piola, A. R., Signorini, S., & McClain, C. R. (2008). Environmental factors controlling the phytoplankton blooms at the Patagonia shelf-break in spring. *Deep-Sea Research Part I*, *55*, 1150–1166. https://doi.org/10.1016/j.dsr.2008.04.011

Genin, A., & Boehlert, G. W. (1985). Dynamics of temperature and chlorophyll structures above a seamount: An oceanic experiment. *Journal of Marine Research*, *43*(4), 907–924. https://doi.org/10.1357/002224085788453868

Guerrero, R. A., Baldoni, A., & Benavides, H. (1999). Oceanographic conditions at the southern end of the Argentine continental slope. INIDEP Doc. Cient., 5, 7–22. Contribution 1083.

Haidvogel, D. B., Beckmann, A., Chapman, D. C., & Lin, R.-Q. (1993). Numerical simulation of flow around a tall isolated seamount. Part II: Resonant generation of trapped waves. *Journal of Physical Oceanography*, *23*(11), 2373–2391. https://doi.org/10.1175/1520-0485(1993)023<2373:NSOFAA>2.0.CO;2

Hill, A .E. (1995). Leakage of barotropic slope currents onto the continental shelf. *Journal of Physical Oceanography*, *25*(7), pp.1617–1621.

Huthnance, J. M. (1978). On coastal trapped waves: Analysis and numerical calculation by inverse iteration. *Journal of Physical Oceanography*, *8*(1), 74–92. https://doi.org/10.1175/1520-0485(1978)008<0074:OCTWAA>2.0.CO;2

Large, W. G., McWilliams, J. C., & Doney, S. C. (1994). Oceanic vertical mixing: A review and a model with a nonlocal boundary layer parameterization. *Reviews of Geophysics*, *32*(4), 363–403. https://doi.org/10.1029/94RG01872

Ledwell, J. R., Montgomery, E. T., Polzin, K. L., Laurent, L. S., Schmitt, R. W., & Toole, J. M. (2000). Evidence for enhanced mixing over rough topography in the abyssal ocean. *Nature*, *403*(6766), 179–182. https://doi.org/10.1038/35003164

Loder, J. W. (1980). Topographic rectification of tidal currents on the sides of Georges Bank. *Journal of Physical Oceanography*, *10*(9), 1399–1416. https://doi.org/10.1175/1520-0485(1980)010<1399:TROTCO>2.0.CO;2

Lueck, R. G., & Mudge, T. D. (1997). Topographically induced mixing around a shallow seamount. *Science*, *276*(5320), 1831–1833. https://doi.org/10.1126/science.276.5320.1831

Lynch, D. R., Ip, J. T. C., Naimie, C. E., & Werner, F. W. (1996). Comprehensive coastal circulation model with application to the Gulf of Maine. *Continental Shelf Research*, *16*(7), 875–906. https://doi.org/10.1016/0278-4343(95)00028-3

Marchesiello, P., McWilliams, J. C., & Shchepetkin, A. (2001). Open boundary conditions for long term integration of regional oceanic models. *Ocean Modelling*, *3*(1-2), 1–20. https://doi.org/10.1016/S1463-5003(00)00013-5

Matano, R. P., Combes, V., Piola, A. R., Guerrero, R., Palma, E. D., Strub, P. T., et al. (2014). The salinity signature of the cross-shelf exchanges in the Southwestern Atlantic Ocean: Numerical simulations. *Journal of Geophysical Research: Oceans*, *119*, 7949–7968. https://doi.org/10.1002/2014JC010116

Matano, R. P., & Palma, E. D. (2008). On the upwelling of downwelling currents. *Journal of Physical Oceanography*, *38*(11), 2482–2500. https://doi.org/10.1175/2008JPO3783.1

Matano, R. P., & Palma, E. D. (2018). Seasonal variability of the oceanic circulation in the Gulf of San Jorge, Argentina. *Oceanography*, *31*(4), 16–24. https://doi.org/10.5670/oceanog.2018.402

Matano, R. P., Palma, E. D., & Piola, A. R. (2010). The influence of the Brazil and Malvinas Currents on the southwestern Atlantic Shelf circulation. *Ocean Science*, *6*(4), 983–995. https://doi.org/10.5194/os-6-983-2010

Matano, R. P., Schlax, M. G., & Chelton, D. B. (1993). Seasonal variability in the southwestern Atlantic. *Journal of Geophysical Research*, *98*(C10), 18,027–18,035. https://doi.org/10.1029/93JC01602

Meredith, M. P., Watkins, J. L., Murphy, E. J., Cunningham, N. J., Wood, A. G., Korb, R., et al. (2003). An anticyclonic circulation above the northwest Georgia rise, Southern Ocean. *Geophysical Research Letters*, *30*(20), 2061. https://doi.org/10.1029/2003GL018039

Miller, R. N., Matano, R. P., & Palma, E. D. (2011). Shelfbreak upwelling induced by alongshore currents: Analytical and numerical results. *Journal of Fluid Mechanics*, *686*, 239–249. https://doi.org/10.1017/jfm.2011.326

Mohn, C., & Beckmann, A. (2002). Numerical studies on flow amplification at an isolated shelfbreak bank, with application to Porcupine Bank. *Continental Shelf Research*, *22*(9), 1325–1338. https://doi.org/10.1016/S0278-4343(02)00004-3

Naimie, C. E., Loder, J. W., & Lynch, D. R. (1994). Seasonal variation of the three-dimensional residual circulation on Georges Bank. *Journal of Geophysical Research*, *99*(C8), 15,967–15,989. https://doi.org/10.1029/94JC01202

Palma, E. D., Matano, R. P., & Piola, A. R. (2004). A numerical study of the southwestern Atlantic Shelf circulation: Barotropic response to tidal and wind forcing. *Journal of Geophysical Research*, *109*, C08014. https://doi.org/10.1029/2004JC002315

Phillips, O. M. (1970). On flows induced by diffusion in a stable stratified fluid. *Deep Sea Research*, *17*(3), 435–443. https://doi.org/10.1016/0011-7471(70)90058-6

Piola, A. R., & Gordon, A. L. (1989). Intermediate waters in the southwest South Atlantic. *Deep Sea Research Part A: Oceanographic Research Papers*, *36*(1), 1–16. https://doi.org/10.1016/0198-0149(89)90015-0

Roberts, D. G., Hogg, N., Bishop, D. G., & Flewellen, C. G. (1974). Sediment distribution around moated seamounts in the Rockall Trough. *Deep Sea Research*, *21*(3), 175–184. https://doi.org/10.1016/0011-7471(74)90057-6

Rogers, A. D. (1994). The biology of seamounts. In Advances in marine biology (Vol. *30*, pp. 305–350). Academic Press.

Romero, S. I., Piola, A. R., Charo, M., & García, C. E. (2006). Chlorophyll-*a* variability off Patagonia based on SeaWiFS data. *Journal of Geophysical Research*, *111*, C05021. https://doi.org/10.1029/2005JC003244

Schär, C., & Davies, H. C. (1988). Quasi-geostrophic stratified flow over isolated finite amplitude topography. *Dynamics of Atmospheres and Oceans*, *11*(3-4), 287–306. https://doi.org/10.1016/0377-0265(88)90003-6

Schetjer, L., Rimondino, C., Chiesa, I., Astarloa, J., Doti, B., Elias, R., et al. (2016). Namuncurá marine protected area: An oceanic hotspot of benthic biodiversity at Burdwood Bank, Argentina. *Polar Biology*, *39*, 2372–2386. https://doi.org/10.1007/s00300-016-1913-2

Strub, P. T., James, C., Combes, V., Matano, R. P., Piola, A. R., Palma, E. D., et al. (2015). Altimeter-derived seasonal circulation on the southwest Atlantic shelf: 278–438°S. *Journal of Geophysical Research: Oceans*, *120*, 3391–3418. https://doi.org/10.1002/2015JC010769

Toole, J. M., Schmitt, R. W., & Polzin, K. L. (1997). Near-boundary mixing above the flanks of a mid latitude seamount. *Journal of Geophysical Research*, *102*(C1), 947–959. https://doi.org/10.1029/96jc03160

Von Stackelberg, U., von Rad, U., & Zobel, B. (1979). Asymmetric sedimentation around Great Meteor Seamount (North Atlantic). *Marine Geology*, *33*(1-2), 117–132. https://doi.org/10.1016/0025-3227(79)90135-X

White, M., & Mohn, C. (2004). Seamounts: a A review of physical processes and their influence on the seamount ecosystem. OASIS Report contract (38).

Wright, D. G., & Loder, J. W. (1985). A depth-dependent study of the topographic rectification of tidal currents. *Geophysical and Astrophysical Fluid Dynamics*, *31*(3-4), 169–220. https://doi.org/10.1080/03091928508219269